THE EXPERIMENTAL DETERMINATION OF EQUILIBRIUM Si ISOTOPE FRACTIONATION FACTORS AMONG $H_4SiO_4^{°}$, $H_3SiO_4^{-}$ AND AMORPHOUS SILICA ($SIO_2 \bullet 0.32\ H_2O$) AT 25 AND 75 ^{O}C USING THE THREE-ISOTOPE METHOD

Franziska M. Stamm[a], Thomas Zambardi[b], Jérôme Chmeleff[a], Jacques Schott[a], Friedhelm von Blanckenburg[c], Eric H. Oelkers[a,d]

a Géosciences Environnement Toulouse, CNRS-UPS-OMP, 14 av. Édouard Belin, 31400 Toulouse, France

b LEGOS, Laboratoire d'Etudes en Géophysique et Océanographie Spatiales (CNRS/UPS/CNES/IRD), Observatoire Midi-Pyrénées14 Avenue Edouard Belin, 31400 Toulouse, France

c GFZ German Research Centre for Geosciences, Potsdam, Germany

d Department of Earth Sciences, UCL, Gower Street, WC1E 6BT London, United Kingdom

19

20 ABSTRACT

21 The accurate interpretation of Si isotope signatures in natural systems requires knowledge of

22 the equilibrium isotope fractionation between Si bearing solids and the dominant Si-bearing

23 aqueous species. Aqueous silicon speciation is dominated by silicic acid ($H_4SiO_4^o$) in most

24 natural aqueous fluids at pH <8.5, but forms $H_3SiO_4^-$, $H_2SiO_4^{2-}$, and polymeric Si species in

25 more alkaline fluids. In this study isotope exchange experiments were performed at *bulk*

26 *chemical* equilibrium between amorphous silica ($SiO_2 \bullet 0.32\ H_2O$) and inorganic aqueous

27 fluids at pH ranging from 5.8 to 9.9 at 25° and 75°C with experiments running as long as 375

28 days. The 'three-isotope method' was used to quantify the equilibrium Si isotope

29 fractionation, $\Delta_{eq}^{30}Si$, between amorphous silica and aqueous Si; at pH ~ 6 this equilibrium

30 fractionation factor was found to be 0.45 ± 0.2 ‰ at 25°C, and 0.07 ± 0.6 ‰ at 75°C. At more

31 basic pH (> 9), equilibrium Si isotope fractionation factors between solid and aqueous

32 solution are higher, at 1.63 ± 0.23 ‰ at 25°C, and 1.06 ± 0.13 ‰ at 75°C. Taking account of

33 the distribution of the aqueous Si species, equilibrium Si isotope fractionation factors between

34 $H_3SiO_4^-$ and $H_4SiO_4^o$ of -2.34 ± 0.13 ‰ and -2.21± 0.05 ‰ at 25 and 75°C, respectively, were

35 determined. The distinct equilibrium isotope fractionation factors of $H_3SiO_4^-$ and $H_4SiO_4^o$, and

36 its variation with temperature can be used to establish paleo-pH and temperature proxies. The

37 application of the three-isotope method also provides insight into the rates of isotopic

38 exchange. For the solid grain size used (~20 nm), these rates match closely the measured bulk

39 dissolution rates for amorphous silica for most of the isotope exchange process, suggesting

40 the dominant and rate controlling isotope exchange mechanism in the experiments is

41 detachment and reattachment of material at the amorphous silica surface.

42

1. INTRODUCTION

Silicon stable isotopes have been used as a tracer of a number of Earth (near-) surface processes, including weathering, biological activity, and marine paleo-temperature (e.g. De La Rocha et al., 1998; Ding et al., 2005; Ziegler et al., 2005a; Opfergelt et al., 2006, 2010, 2012, 2017; Georg et al., 2007; De La Rocha et al., 2011; Demarest et al., 2009; Hendry et al., 2011; Hendry and Robinson, 2012; Pogge von Strandmann et al., 2012; Pokrovsky et al., 2013; Marin-Carbonne et al., 2014; Oelze et al., 2014; Frings et al., 2015; He et al., 2016). The Si isotopic composition of many terrestrial reservoirs have been measured, including that of oceans, lakes, rivers and groundwaters (e.g. De La Rocha et al., 2000, 2011; Wischmeyer et al., 2003; Reynolds et al., 2006; Georg et al., 2009; Ding et al., 2011; Grasse et al., 2013; Pokrovsky et al., 2013; Frings et al., 2015), soils (Riotte et al., 2018a), plants (Douthitt, 1982; Ding et al., 2008a, 2008b; Pogge von Strandmann et al., 2012; Opfergelt et al., 2012; Riotte et al., 2018b), minerals, sedimentary rocks, cherts, and banded iron formations (e.g. Douthitt, 1982; Ziegler et al., 2005a, 2005b; Georg et al., 2009; Steinhoefel et al., 2010; van den Boorn et al., 2010; Savage et al., 2013). Constraining isotopic fractionation among these reservoirs is crucial to understanding the Si geochemical cycle.

Experimental studies have demonstrated that the Si isotopic signatures in natural environments can evolve during mineral precipitation (Li et al., 1995; Basile-Doelsch et al., 2005; Geilert et al., 2014, 2015; Roerdink et al., 2015; Oelze et al., 2015), mineral dissolution (Delvigne et al., 2012) or during adsorption of aqueous species (Delstanche et al., 2009; Oelze et al., 2014). Silicon isotopic fractionation during such mineral-aqueous fluid reactions in nature have been considered to be influenced by kinetic isotope fractionation (Geilert et al., 2014; Oelze et al., 2015; Roerdink et al., 2015; Poitrasson, 2017). However the degree of Si isotope fractionation at equilibrium is scarcely known, so that the relative impact of kinetic versus equilibrium processes on Si isotope fractionation during fluid-mineral interactions cannot be assessed unambiguously.

A critical factor to determine the equilibrium fractionation between a mineral and its coexisting aqueous fluid is the aqueous speciation of the system. The impact of aqueous speciation on the mineral/fluid fractionation factor has been demonstrated for elements such as boron, carbon, magnesium, mercury, transition metals and silicon (Hemming and Hanson, 1992; Zhang et al., 1995; Zeebe, 2005; Klochko et al., 2006, 2009; Asael et al., 2009; Holloway et al., 2011; Jiskra et al., 2012; Ryan et al., 2013; Yin et al., 2013; Fujii et al., 2014,

75   2015; Dupuis et al., 2015; Noireaux et al., 2015; Schott et al., 2016; Balan et al., 2018;

76   Mavromatis et al., 2019). Aqueous Si speciation depends on the solution pH and total

77   dissolved Si concentration. In inorganic systems at ambient temperature, pH < 8.5 and $m_{Si} \leq$

78    $10^{-2.7}$ M (~ amorphous silica solubility), silicic acid ($H_4SiO_4^o$) dominates Si aqueous

79   speciation. As pH increases, the species, $H_3SiO_4^-$ and $H_2SiO_4^{2-}$, form at the expense of silicic

80   acid, whereas polymeric Si species become increasingly important in aqueous solutions

81   supersaturated with respect to amorphous silica (Dietzel, 2000). At 75 ^{o}C, $H_4SiO_4^o$ will

82   dominate only up to pH 7.8, where the species $H_3SiO_4^-$ starts form at the expense of aqueous

83   silicic acid. Figure 1 shows the speciation of Si in an aqueous solution containing 1.6×10^{-3} M

84   Si (corresponding to the equilibrium with amorphous silica at pH<9) as a function of pH for

85   25°C and 75°C, respectively. As the speciation of aqueous silicon changes with pH,

86   equilibrium Si isotope fraction between this fluid and any Si bearing mineral will change

87   accordingly (Dupuis et al., 2015; Fujii et al., 2015).

88   Several past studies attempted to determine Si fractionation factors between

89   amorphous silica and its coexisting aqueous solutions (Geilert et al., 2014; Oelze et al., 2014;

90   Roerdink et al., 2015). Most report an enrichment of the solid in light (^{28}Si) isotopes, which

91   could be explained by non-equilibrium fractionation during precipitation of amorphous silica

92   from a supersaturated solution (Dupuis et al., 2015). Zheng et al. (2016) measured Si isotopic

93   fractionation at chemical equilibrium between a Fe(III)-bearing silica gel and artificial

94   Archean seawater; they reported a 25°C equilibrium fractionation factor, $\Delta_{eq}^{30}Si_{gel\text{-}fluid}$ of ~ -

95   3.5 ‰. Dupuis et al. (2015) used first-principle methods to calculate the 25 °C equilibrium

96   fractionation factors between quartz and its co-existing aqueous solution, and kaolinite and its

97   co-existing aqueous solution. These calculations predict a $\Delta_{eq}^{30}Si_{mineral\text{-}fluid}$ at neutral pH of

98   2.1 ± 0.2‰ and 0.4 ± 0.2‰, for the quartz-aqueous solution and kaolinite-aqueous solution

99   system, respectively. Additionally these authors reported the 25°C equilibrium Si isotope

100   fractionation factor, $\Delta_{eq}^{30}Si_{H_3SiO_4^- - H_4SiO_4^o}$ = -1.6 ± 0.3‰, between the $H_3SiO_4^-$ and $H_4SiO_4^0$

101   aqueous silicon species. Similarly, Fujii et al. (2015) experimentally and theoretically

102   determined the equilibrium fractionation factor between the two aqueous species $H_3SiO_4^-$ and

103   $H_4SiO_4^0$. Their determined values of $\Delta_{eq}^{30}Si_{H_3SiO_4^- - H_4SiO_4^o}$ = -3.5 ‰ (experimental) and

104   $\Delta_{eq}^{30}Si_{H_3SiO_4^- - H_4SiO_4^o}$ = -3 ‰ (ab initio calculations) are somewhat inconsistent with those

105   calculated by Dupuis et al. (2015). These inconsistencies between the ab initio results of Fujii

106   et al. (2015) and Dupuis et al. (2015) stem from the models used for the configuration of the

107   Si aqueous species in solution. Fujii et al. (2015) assumed the aqueous Si consisted of static

108   isolated clusters, whereas Dupuis et al. (2015) took into account the interactions of these

109   clusters with surrounding water molecules as well as the configurational disorder of the

110   solution.

111   The aim of this study is to expand on these past efforts, by determining experimentally

112   the equilibrium fractionation factors between amorphous SiO_2 and the aqueous Si species

113    $H_3SiO_4^-$ and $H_4SiO_4^0$ as a function of pH over a range of 5.8<pH<10 at temperatures of 25°C

114   and 75°C. Experiments were performed at pH ~6, as silicic acid $H_4SiO_4^0$ will be the only

115   silica species present in solution, and at pH ~9 where, in addition to $H_4SiO_4^0$, sufficient

116    $H_3SiO_4^-$ is present but the presence of $H_2SiO_4^{2-}$ and potentially forming Si-O polymer species

117   are insignificant. Results at these conditions will, therefore, allow the unambiguous

118   determination of distinct equilibrium fractionation factors among amorphous SiO_2 and

119   aqueous $H_3SiO_4^-$ and $H_4SiO_4^0$. To assure the attainment of isotopic equilibrium, the 'three-

120   isotope method' was applied. The purpose of this paper is to report the results of this

121   experimental study and provide new insights into how aqueous solution speciation and

122   temperature can affect the Si equilibrium isotopic fractionation between amorphous silica and

123   an aqueous solution.

124   **2. THEORETICAL BACKGROUND**

125   **2.1 Geochemical calculations of amorphous silica dissolution rates**

126   All geochemical calculations in this study were performed using PHREEQC

127   (Parkhurst and Appelo, 2013) together with its llnl thermodynamic database. The standard

128   state adopted in this study calls for unit activity of pure minerals, solids, and H_2O. For

129   aqueous species, the standard state is unit activity of a 1 molal solution extrapolated to infinite

130   dilution. The activity coefficients of charged aqueous species were calculated using the

131   Davies equation, whereas the activity coefficients of neutral species were assumed to be equal

132   to one.

133   The experiments in the present study were begun by first equilibrating an initially Si

134   free aqueous solution of known pH with amorphous silica. The dissolution reaction for

135   amorphous silica is described by:

136    $$SiO_{2,am} + 2\,H_2O \rightarrow H_4SiO_4^0 \tag{1}$$

137   The law of mass action for reaction (1) is given by

138 $$K_{eq} = \frac{a_{H_4SiO_4^0}}{a_{SiO_2,am}\,a_{H_2O}^2}$$ (2)

139 where K_{eq} stands for an equilibrium constant and a_i refers to the activity of the subscripted

140 species or phase. Taking account of this standard state, in pure water

141 ($a_{H_4SiO_4^0} = C_{H_4SiO_4^0}$, where C_i stands for the concentration of the subscripted species), Eqn.

142 (2) reduces to

143 $$K_{eq} = C_{H_4SiO_4^0,eq}$$ (3)

144 where $C_{H_4SiO_4^0,eq}$ stands for the concentration of $H_4SiO_4^0$ in equilibrium with amorphous silica.

145 The surface area normalised rates of amorphous silica dissolution (r) in a closed system and in

146 the absence of specific inhibitors or catalysts can be described using (Rimstidt and Barnes,

147 1980)

148 $$r = \frac{dC_{H_4SiO_4^0}}{dt} = S/M\left(k_+ - k_- C_{H_4SiO_4^0}\right)$$ (4)

149 where S and M refer to the interfacial surface area and mass of aqueous solution in the reactor

150 and k_+ and k_- designates amorphous silica dissolution and precipitation rate constants,

151 respectively. Note $C_{H_4SiO_4^0}$ in Eqn. (4) has units of mol/kg H_2O. Rearranging Eqn. (4) and

152 integrating it between times $t = 0$ and t gives

153 $$t = (1/k'_-)ln\left(\frac{k'_+ - k'_- C_{H_4SiO_4^0}}{k'_+ - k'_- C_{(H_4SiO_4^0)_0}}\right)$$ (5)

154 where $k'_+ = (\frac{S}{M})k_+$ and $k'_- = (\frac{S}{M})k_-$, and $C_{(H_4SiO_4^0)_0}$ denotes $C_{H_4SiO_4^0}$ at time zero. When

155 starting from a zero concentration of $H_4SiO_4^0$ in solution, Eqn. (5) reduces to

156 $$t = (1/k'_-)ln\left(\frac{k'_+ - k'_- C_{H_4SiO_4^0}}{k'_+}\right).$$ (6)

157 Noting that $\frac{k'_+}{k'_-} = C_{(H_4SiO_4^0)_{eq}}$, where $C_{(H_4SiO_4^0)_{eq}}$ again denotes the concentration of dissolved

158 silica in equilibrium with amorphous silica, the temporal evolution of dissolved silica

159 concentration in the closed system is described by

160 $$C_{H_4SiO_4^0} = C_{(H_4SiO_4^0)_{eq}}\left(1 - e^{-tk'_-}\right)$$ (7)

161

6

2.2. Si isotope systematics

Silicon isotope compositions in this study are reported using the standard δ-notation in per mil (‰) relative to the international NBS-28 standard (NIST RM-8546), computed using:

$$\delta^x Si = \left[\frac{(^x Si/^{28}Si)_{Sample}}{(^x Si/^{28}Si)_{NBS-28}} - 1 \right] \tag{8}$$

where $(^x Si/^{28}Si)_{Sample}$ refers to the atomic ratio of the Si with mass x, which denotes either ^{29}Si or ^{30}Si, to that of ^{28}Si in the sample of interest. The Si isotopic fractionation factor between a solid and an aqueous fluid $(\alpha^{x/28}_{solid-fluid})$ is defined as:

$$\alpha^{x/28}_{solid-fluid} = \frac{(^x Si/^{28}Si)_{solid}}{(^x Si/^{28}Si)_{fluid}} \tag{9}$$

The silicon isotopic fractionation between a solid and a coexisting aqueous phase can be also described using $\Delta^x Si_{solid-fluid}$, which is defined by

$$\Delta^x Si_{solid-fluid} = \delta^x Si_{solid} - \delta^x Si_{fluid} \tag{10}$$

Note that $\Delta^x Si_{solid-fluid}$ is approximately related to $\alpha^{x/28}_{solid-fluid}$ by

$$\Delta^x Si_{solid-fluid} \approx 10^3 ln\alpha^{x/28}_{solid-fluid} . \tag{11}$$

The fractionation factor between the solid and the aqueous fluid depends on the proportion of the different species, i, present in this fluid and their individual fractionation factors with the solid, $\alpha^{x/28}_{solid-i}$, consistent with (Zhang et al., 1995):

$$10^3 ln\alpha^{x/28}_{solid-fluid} = \sum_i (x_i \times 10^3 ln\alpha^{x/28}_{solid-i}) \tag{12}$$

where x_i refers to the mole fraction of the dissolved Si present in the ith aqueous species.

2.3. Three-isotope method

Equilibrium fractionation factors in the present study were generated using the three-isotope method. The three-isotope method was originally used to determine the equilibrium isotopic fractionation factors of oxygen between mineral and co-existing aqueous solutions (Matsuhisa et al., 1978; Matthews et al., 1983a, 1983b, 1983c). Over the past 10 years, this method was also successfully applied to non-traditional isotopic systems, such as Mg and Fe (Shahar et al., 2008; Beard et al., 2010; Li et al., 2011; Frierdich et al., 2014; Reddy et al., 2015), as well as to Si (Zheng et al., 2016). This approach has also been used to evaluate the

189   kinetics of isotopic exchange reactions between two components (Cole and Chakraborty,

190   2001; Johnson et al., 2002; Li et al., 2011; Wu et al., 2012; Zheng et al., 2016). Before

191   exchange, one component (Phase A, typically the solid) exhibits a "natural" isotopic

192   composition and plots on a δ vs. δ diagram, such as Fig. 2, on a primary fractionation line,

193   also known as the terrestrial fractionation line (TFL). This line follows a mass-dependent

194   relation where $\delta^{30}Si \approx 1.93 \times \delta^{29}Si$ (Young et al., 2002). The second component (Phase B,

195   typically the fluid) is enriched in one isotope (for example, ^{29}Si in the present study) and thus

196   has a distinct and known offset from the TFL. As the system undergoes isotopic exchange, the

197   isotopic compositions of the two components will gradually evolve over time (t) towards

198   isotopic equilibrium. Once the isotopic exchange is complete and isotopic equilibrium has

199   been attained, the isotopic compositions of the two phases will fall on a secondary

200   fractionation line (SFL) parallel to the TFL. The position of the SFL can be determined from

201   the isotopic mass balance of the system (see Fig. 2).

202   For many systems, isotopic exchange is slow and therefore often incomplete. The

203   three-isotope method, nevertheless, allows for the determination of *equilibrium fractionation*

204   *factors* through the determination of the degree of isotope exchange (F). The degree of

205   isotopic exchange is defined by

206      $$F = \frac{(\delta_t - \delta_i)}{|\delta_e - \delta_i|}$$ (13)

207   where δ_t denotes the isotopic composition of either one of the phases at any time, t, during the

208   isotope exchange reaction, and δ_i and δ_e describe the initial and equilibrium isotopic

209   composition of this phase. The parameter F ranges from 0 to 1 as isotopic equilibrium is

210   attained. In a two-component system δ_e can be derived from the mass balance constraints

211   (Zheng et al., 2016), and calculated from

212      $$\delta_e = \delta_{mean} - \left(\frac{N_{solid}}{N_{solid} + N_{fluid}}\right) \times \Delta_{eq,solid-fluid}$$ (14)

213   where δ_{mean} in this study stands for the mass averaged Si isotope composition of the system,

214      $\Delta_{eq,solid-fluid}$ designates the *equilibrium isotope fractionation factor* between the solid and

215   fluid phases, and N_{solid} and N_{fluid} denote the number of moles of Si in the solid and fluid phase,

216   respectively. If the $\Delta_{eq,solid-fluid}$ of the system is not known, as is the case in the present

217   study, it can be obtained from an iterative fit of experimental data (Zheng et al., 2016).

218

2.4. Kinetics of isotopic exchange

The 'three-isotope method' not only allows determination of the equilibrium fractionation factors of a solid-fluid system, but also allows determination of the kinetics of isotopic exchange. Following the approach of Cole and Chakraborty (2001) and Johnson et al. (2002) isotope exchange rates can be quantified using

$$\frac{-d(1-F)}{dt} = k_n(1-F)^n \tag{15}$$

where k_n stands for the rate constant of reaction order n, this reaction order is usually an integer from 0 to 3. Isotope exchange reactions typically follow either a first-order ($n=1$) or second-order ($n=2$) rate law (Criss et al., 1987; Huang and Tsai, 1970; Johnson et al., 2002; Welch et al., 2003; Li et al., 2011; Zheng et al., 2016). The integrated form of this rate equation can be written as either

$$\ln(1-F) = -k_1 t \tag{16}$$

for $n=1$

$$\frac{F}{(1-F)} = k_2 t \tag{17}$$

for $n=2$.

Isotope exchange rate constants can be quantified by fitting the experimental value of F to Eqn. (16) for the first order rate constant or Eqn. (17) for the second order rate constant (Cole and Chakraborty, 2001; Johnson et al., 2002; Li et al., 2011).

237

3. METHODS

3.1. Experimental approach

3.1.1. Starting powder - amorphous silica

All experiments in the present study were performed in series using Alpha Aeser® 100 mesh hydrated silicic acid powder. This powder was cleaned prior to each experimental series by sedimentation in >18.2 Ω de-ionized water (Milli-Q®) to remove ultrafine particles (Pokrovski and Schott, 1998). In each case, from 40 to 75 g of the hydrated silicic acid powder was suspended by stirring in a 1dm³ glass beaker. The powder was sedimented for 10 minutes and then decanted. This operation was repeated until the supernatant became clear within the first 5 min. Subsequently the powder was oven dried at 60°C. To avoid hydration

of the powder it was placed into a desiccator while it cooled to room temperature. Representative scanning electron microscope (SEM) and transmission electron microscope (TEM) images of the resulting powders are shown in Fig. 3A and B. These images were acquired using a MEB JEOL JSM-7800F Prime electron microscope and a JEOL JEM-ARM200F Cold FEG transmission electron microscope at the Raimond Castaing Microcharacterization Centre (Toulouse, France), respectively. The TEM images were used to measure average grain size with the ImageJ software package (Schindelin et al., 2012); the average measured grain size of the cleaned dried amorphous silica was ~21 ± 5 nm (2SD, n=100). Energy dispersive spectroscopy (EDS) analyses indicate the prepared powder contained no metals other than Si. Thermogravimetric analyses, performed with a Mettler Toledo® ATG/DSC1, showed that the powders also contained ~8.7 % H_2O, which is consistent with the chemical formula $SiO_2 \bullet 0.32 \ H_2O$. The specific surface areas of the cleaned amorphous silica were determined with a Quantachrome Autosorb-1MP using the nitrogen multipoint BET method (Brunauer et al., 1938). The average surface area of the initial amorphous silica powders is 196.3 m^2/g, and ranged from 175 m^2/g to 215 m^2/g with an estimated uncertainty of ± 10%.

3.1.2. Initial aqueous solutions

The initial aqueous solutions used in the experiments were prepared using high purity de-ionized Milli-Q® water (>18.2 Ω), and reagent grade HCl, NH_4OH and NH_4Cl; the compositions of these initial solutions are provided in Table 1. These solutions had a pH of ~6 and ~10 for the 25°C experiments and ~6 and ~9 for the 75°C experiments; experiments run with these fluids are labelled SibA, SicB, SigA, and SikB, respectively. The pH of these fluids were selected as at pH < 8.5 for 25°C and pH < 7.8 at 75°C, aqueous silicic acid ($H_4SiO_4^o$) will be the only significant silica species present in solution. At pH 9.9 at 25°C and 9.1 at 75°C, aqueous $H_3SiO_4^-$ will have formed at the expense of aqueous silicic acid and both will have a similar species distribution of ~50% $H_4SiO_4^o$ and ~50% $H_3SiO_4^-$. This enables quantification of the effect of the aqueous $H_3SiO_4^-$ species on equilibrium fractionation factors at these two temperatures.

3.1.3. Characterization of the aqueous solutions

The aqueous solution pH was regularly monitored during the experiments with a Metrohm® 913 pH Meter connected to a standard glass microelectrode. This electrode was

281   calibrated using certified Orion Thermo Scientific® buffers. The uncertainty in the

282   measurements was determined to be 0.05, equal to 2 standard deviations of ~40 repeated

283   measurements of the pH=4.01 calibration standard. For experiments at 75°C, the pH was

284   measured at 25°C and later calculated to this higher temperature with PHREEQC.

285   Aqueous silicon concentrations were determined by the molybdate blue method

286   (Truesdale and LeCorre, 1975) using a Bran & Luebbe® analyser-III colorimeter coupled to a

287   Seal XY-2 autosampler and a Technicon analyser II mixing unit. The measurements were

288   conducted over the 0.1 to 10 ppm concentration range. The long-term reproducibility of these

289   measurements was determined to be within 3% and the quantification limit was 0.04 ppm. To

290   verify that aqueous Si polymerisation did not occur in the reactive fluids during the

291   experiments, additional Si concentration measurements were performed on selected fluid

292   samples by ICP-OES. In all cases the aqueous Si concentrations measured by ICP-OES were

293   equal to within uncertainty of corresponding values measured by colorimetry confirming that

294   silica polymerisation was negligible.

295

296   *3.1.4. Experiment design: Step 1 Equilibration of reactive fluids*

297   Experiments in this study were conducted in four distinct series. Each series began by

298   equilibrating 200 ml of an initial aqueous fluid with 3 g of pre-washed amorphous SiO_2

299   powder in closed polypropylene bottles (see Table 1). Once closed, these bottles were placed

300   in shaking thermostatic baths at either ~25°C or ~75°C. The aqueous fluids in the bottles were

301   sampled 8 times at regular intervals during the 19 to 65 days of this equilibration step. The pH

302   was measured immediately after each sampling at room temperature. The samples collected

303   from the 75°C experiments were then diluted to prevent precipitation. Aqueous Si

304   concentrations were determined by colorimetry on all samples and by ICP-OES on selected

305   samples. Chemical equilibrium was assumed to be reached when both pH and the Si

306   concentration of the aqueous solutions attained constant values within uncertainty. This initial

307   step was stopped once these constant values were reached. The fluids were then filtered with

308   Merck® 0.2 μm Teflon syringe filters. Fluids recovered from the 75°C experiments were kept

309   in the thermostatic bath until subsequently used in the isotopic exchange experiments

310   described below.

311

312 *3.1.5. Experiment design: Step 2 Isotopic exchange experiments*

313   The four chemical equilibrated fluids were enriched with a ^{29}Si isotope tracer to obtain

314 a δ^{29}Si $= \sim 23$‰ (see Table 2). The added ^{29}Si isotope tracer was prepared by dissolving

315 Eursio-top$^{®}$ ^{29}SiO$_2$ powder, having an initial composition of 0.21% ^{28}Si, 99.76% ^{29}Si, and

316 0.03% ^{30}Si in de-ionized water. After the addition of this spike to the equilibrated fluids, the

317 Si concentration and pH were measured. The fluid pH was adjusted, if necessary, by adding a

318 small quantity of HCl or NH$_4$OH to assure these initial fluids were as close to equilibrium

319 with amorphous silica as possible. Each series of isotopic exchange experiments consisted of

320 a suite of 8 closed system experiments of the selected durations listed in Table 2. This

321 approach was selected so that both the solids and fluids could be collected and analysed after

322 these distinct experiment durations. The overall duration of each experimental series were

323 selected so that degree of isotopic exchange would approach 1 at the end of each series. Each

324 individual experiment was performed in 10 ml polypropylene reactors. Into each reactor was

325 added ~ 0.15 g of amorphous SiO$_2$ powder with a known Si isotope composition and 5 ml of

326 the prepared ^{29}Si enriched fluid. The 25°C experiments were placed into an orbital shaker to

327 be constantly mixed. The 75°C experiments were placed into a thermostatic bath and hand

328 shaken once or twice a day. To verify that no leakage occurred during any experiment, all

329 reactors were weighted both at the beginning and the end of each experiment. At pre-chosen

330 time intervals, a reactor was centrifuged for 20 min at 4500 rpm and then opened. The

331 supernatant was separated from the powder and filtered using Merck$^{®}$ 0.2 μm Teflon syringe

332 filters. The pH was measured immediately after sampling, and fluids recovered from the 75°C

333 experiments were diluted just after measuring pH. The recovered powder was gently rinsed

334 with de-ionized water on a 0.2 μm filter, oven-dried at 40°C, and stored for further analysis. It

335 is unlikely that this rinsing altered significantly the isotopic composition of the recovered

336 solid due to the low solubility and dissolution kinetics of the solid.

337

338 **3.2. Si isotope analysis**

339   Silicon isotope compositions were measured in the fluid and solid samples collected

340 from all isotope exchange experiments, as well as the initial washed SiO$_2$ powders, the spiked

341 initial fluid and the non-spiked chemical equilibrated fluids. Aqueous samples were prepared

342 by first acidifying the solutions using bi-distilled 3N HCl to pH $\sim$2. Amorphous silica

343 powders were processed using the alkali fusion method described by Zambardi and

344 Poitrasson (2011). From 2 to 5 mg of the solids were weighted into silver crucibles (XRF

345   scientific, Montreal, Canada) together with a ~200 mg Merck® NaOH pellet. The crucibles

346   were capped and placed into a furnace heated at 720°C for 10 min. They were subsequently

347   cooled to room temperature and placed into 30 cm³ Savillex® Teflon beakers filled with 20 ml

348   Milli-Q® water for 24 hours to dissolve the fusion cake. The resulting fluids were then

349   transferred to 60 cm³ polypropylene bottles and diluted to 40 ml by adding Milli-Q® water.

350   These 40 ml samples were then acidified using ~10 N bi-distilled HCl to obtain a pH of 1.5.

351   All prepared Si-bearing fluids generated from either the solid or fluid samples were

352   purified by cation-exchange chromatography using the Bio-Rad® AG50W-12X cationic resin

353   (Georg et al., 2006; Zambardi and Poitrasson, 2011). The detailed cleaning procedure of the

354   resin is described in Zambardi and Poitrasson (2011). From 0.5 to 2 ml of prepared fluids

355   containing up to 70 µg Si were loaded, directly collected, and eluted twice with Milli-Q®

356   water to obtain 6 ml samples. These were then diluted and acidified to obtain a 3 ppm solution

357   with a total 0.05 M HCl concentration. Silicon recovery after processing was determined to be

358   between 90 to 100 %. The ^{28}Si signal of the procedural blank, processed in the same way, was

359   found to be less than < 2% and was thus considered as negligible.

360   Silicon isotope ratios were determined using a Thermo Scientific Neptune® MC-ICP-

361   MS either at the Observatoire Midi Pyrenées / Laboratorie Géosciences Environnement

362   Toulouse (GET), France, or the GeoForschungsZentrum (GFZ) in Potsdam, Germany.

363   Measurements were performed in medium resolution under either wet plasma at the GET or

364   dry plasma conditions and the GFZ. Two different methods were used as these analyses were

365   performed in different laboratories, which routinely use different procedures for Si isotope

366   analyses. Measurements performed on several identical samples at these laboratories yielded

367   identical results within uncertainty. The wet plasma samples were introduced with a Thermo

368   SIS system with a double-pass cyclonic spray chamber. An ESI ApexHF desolvator (having

369   sample path made of Perfluoroalkoxy alkane, PFA) and fitted with a PFA nebulizer was used

370   for dry plasma conditions at the GFZ (Schuessler and von Blanckenburg, 2014). The

371   instrumental mass bias drift was corrected using the sample standard bracketing technique

372   relative to NBS-28 (NIST SRM 8546), combined with Mg doping as an internal standard in

373   all measured samples and standards. Measurements of ^{25}Mg/^{24}Mg ratios were performed in

374   the dynamic mode, alternating between Si and Mg isotopes. Russell's exponential law

375   (Russell et al., 1978) was then used to correct for the mass bias drift. The accuracy and

376   precision of the isotopic analysis were validated by repeated measurement of the BHVO-2

377   reference material. They yielded a long-term reproducibility of δ^{30}Si= -0.26 ± 0.13 ‰ for the

378   GET analyses (2 S.D, n=59) and δ^{30}Si= -0.28 ± 0.09 ‰ for the GFZ analyses (2 S.D, n=18),

379 which are in close agreement with measurements reported in previous studies (e.g. Abraham
380 et al., 2008; Zambardi and Poitrasson, 2011; Savage et al., 2013, 2014).

381

382 **4. RESULTS**

383 **4.1 Attainment of fluid-amorphous SiO$_2$ equilibrium during the fluid equilibration step**

384   Each experimental series began by equilibrating the initial Si-free fluids with the pre-
385 treated amorphous SiO$_2$. The temporal evolution of dissolved Si concentration and pH in
386 these fluids are provided in Table A of the electronic supplement; the Si concentrations are
387 also shown in Fig. 4. The Si concentration of the initial fluids at both 25° and 75°
388 systematically increase to a constant maximum value. The constant final Si concentrations
389 were within 10 % of those calculated to be in equilibrium with amorphous SiO$_2$ using
390 PHREEQC. The curve drawn through these measured Si concentrations correspond to a fit of
391 these data to Eqn. (7); the rate constants obtained by this regression are provided in Table 3.

392 **4.2 Results of Isotope exchange experiments**

393 *4.2.1. Observations on the solid phases*

394   SEM and TEM images of amorphous SiO$_2$ collected from the longest duration
395 experiment run of each experimental series were obtained; representative images are provided
396 in Fig. 3 C and D. These images show that these final solids contain only amorphous SiO$_2$,
397 and are identical in appearance to the pre-experiment, pre-treated solids.

398   A summary of the various measured characteristics of the solids collected after the
399 longest duration experiment of each series is provided in Table B of the electronic
400 supplement. The measured grain sizes of the collected final solids were 20 ± 1 nm (n=85,
401 2 S.D.), which are identical, within uncertainty, to the corresponding pre-treated solids. The
402 water content of these final solids was measured at 8.4% by TGA, which is identical within
403 uncertainty to that of the original pre-treated solids. Measured BET surface areas of the final
404 reacted powders are somewhat lower than those of the original pre-treated solids; the largest
405 decreases were those of the final pH 6.4, 25°C experiment and the final pH 9.1, 75°C
406 experiment, which exhibited a decrease of ~35%. This could result from Ostwald ripening
407 affecting the silica grains during the runs. Overall the post-experiment solids, however, appear
408 to have been essentially unchanged by these isotope exchange experiments.

409

14

410 *4.2.2 Chemical and isotopic evolution of the isotope exchange experiments*

411   The temporal evolution of the pH, the bulk Si composition of the fluids, and the fluids

412   and solids Si isotopic compositions during isotopic exchange step of all experimental series

413   are provided in Fig. 5. The pH of the fluids remained close to constant during the

414   experimental series other than during series run at pH 9.1 and 75°C, where the pH decreased

415   somewhat. This decrease could be due to a loss of NH_4OH through evaporation over time

416   from the reactors. Note that pH variations at alkaline conditions will alter the relative

417   importance of the $H_3SiO_4^-$ versus $H_4SiO_4^0$ species in solution. As such the isotopic

418   compositions of the final fluids of this high pH series were not considered in the

419   determination of the equilibrium Si isotope fractionation factors given below. The dissolved

420   Si concentrations remained close to constant during the pH ~6 experiments, but tended to

421   decrease with time during the higher temperature experiments; this decrease is consistent with

422   the observed decrease in pH, which tends to decrease amorphous silica solubility. The $\delta^{29}Si$

423   values of the fluids and solids mirror one another; in each case, the $\delta^{29}Si$ value of the ^{29}Si

424   enriched fluid phase decreases rapidly at the beginning of each experimental series, while the

425    $\delta^{29}Si$ value in the corresponding solid increases. Note that $\delta^{29}Si$ of the solids increase far less

426   than the $\delta^{29}Si$ decreases in the fluid phase. This is due to the relative masses of Si in these

427   phases; there is far more Si present in the solid than in the liquid phase in our experimental

428   systems.

429

430   **4.3. Silicon isotope fractionation factors**

431   The *equilibrium* Si isotope fractionation factors, $\Delta_{eq}^{30}Si_{SiO2,am-fluid,}$ at the conditions of

432   the four experimental series considered in this study were generated with the aid of Fig. 6 as

433   described in section 2.3. The value of $\Delta_{eq}^{30}Si_{SiO2,am-fluid,}$ was estimated from the extrapolation

434   to *F* = 1 of the solid lines drawn though the isotopic data shown in these figures. This fit was

435   aided by the fact that these isotopic exchange reactions approached to within 90% of their

436   final equilibrium compositions; the final values of *F* were 0.91 and 0.98 in these experimental

437   series (see Table 2). A close correspondence can be seen between the isotopic data and these

438   fits. The values of $\Delta_{eq}^{30}Si_{solid-fluid}$ obtained from these fits are provided in Table 4 and vary

439   with temperature and pH. Note that as mentioned above, the final few measurements of the

440   experimental series performed at pH 9.9 and 25°C, and pH 9.1 and 75°C were excluded from

441   the fit due to pH drift; their exclusion affected negligibly the retrieved values of $\Delta_{eq}^{30}Si_{SiO2,am-}$

442 *fluid.* The $\Delta_{eq}^{30}Si_{SiO2,am\text{-}fluid}$ decreases by ~0.4‰ with increasing temperature from 25 to 75°C at

443 pH 6. With increasing pH to ~9, however, the $\Delta_{eq}^{30}Si_{SiO2,am\text{-}fluid}$ increases by 1.0 to 1.2 ‰.

444   The observed $\Delta_{eq}^{30}Si_{SiO2,am\text{-}fluid}$ variation with pH can be attributed to the dependence

445 of aqueous Si speciation on pH. The speciation of Si in the reactive fluids of each series is

446 provided in Table 4. Aqueous Si was present almost exclusively as $H_4SiO_4^0$ in the pH ~6

447 experiments, but as much as 48% of dissolved Si in the pH ~9 experiments was present as the

448 $H_3SiO_4^-$ species – see Fig. 1. In addition to the major aqueous Si species, $H_4SiO_4^0$ and $H_3SiO_4^-$

449 , polymeric Si species represent <5 % of total Si speciation and are hence considered

450 negligible. Therefore $H_4SiO_4^o$ and $H_3SiO_4^-$ are assumed to be 100 % of total Si-speciation in

451 solution. Taking account of Eqns. (10) – (12) and the calculated speciation of Si in the

452 aqueous phase in the experiments, the equilibrium Si isotope fractionation factors between

453 amorphous silica and $H_4SiO_4^0$ or $H_3SiO_4^-$ $(\Delta_{eq}^{30}Si_{SiO2,am-H_4SiO_4^0}$ and

454 $\Delta_{eq}^{30}Si_{SiO2,am-H_3SiO_3^-})$ and between the species $H_3SiO_4^-$ and $H_4SiO_4^0$ $(\Delta_{eq}^{30}Si_{H_3SiO_4^--H_4SiO_4^0})$

455 were determined at both 25° and 75°C. The resulting values are provided in Table 4.

456

4.4. Isotope exchange kinetics

458   The rate of attainment of isotopic equilibrium provides insight into the mechanism of

459 isotope exchange. The temporal evolutions of the degree of isotope exchange, *F*, for the four

460 experimental series in this study are shown in Fig 7. It can be seen that isotope exchange is

461 relatively rapid during the first 10 days of each experimental series. After 10 days, the

462 exchange reaction slows as the system approaches isotopic equilibrium. The curves in this

463 figure were generated using the first order rate law, Eqn. (16), to be consistent with the

464 amorphous SiO_2 rate expression provided by Eqn. (3) to (7). The rate constants used to

465 generate these curves were those retrieved from the amorphous silica dissolution rate

466 experiments run at the beginning of each series – see above and Table 3. It can be seen that

467 the initial isotopic exchange rates shown in Table 5 are similar to- if not faster than- those of

468 the bulk amorphous silica dissolution rates obtained from the first step of each experimental

469 series. As isotopic equilibrium is approached, these isotope exchange rates become slow

470 relative to that calculated from the bulk amorphous silica dissolution rates.

471

5. DISCUSSION

5.1. Silicon isotope fractionation between amorphous silica and aqueous solution

The equilibrium Si isotope fractionation factor between amorphous silica ($SiO_2 \cdot 0.32$ H_2O) and the aqueous solution determined in this study at 25°C and pH 6.4 where $H_4SiO_4°$ accounts for 100% of dissolved silica is $\Delta_{eq}^{30}Si_{SiO2,am\text{-}fluid} = \Delta_{eq}^{30}Si_{SiO2,am - H_4SiO_4°} = $ 0.45 ± 0.20 ‰. This value is identical, within uncertainty with those of Roerdink et al. (2015), who reported a $\Delta_{eq}^{30}Si_{SiO2,am\text{-}fluid}$ of 0.0 ± 1.1 ‰ at 20 °C and 0.5 ± 0.6‰ at 35 °C for this system. Note that these former values were obtained at a pH of 8.5 from amorphous silica precipitation experiments using a surface kinetic model to correct for the effect of precipitation kinetics. Oelze et al. (2014) proposed a $\Delta_{eq}^{30}Si_{SiO2,am\text{-}fluid}$ of -0.3 ‰ from experiments measuring the adsorption of silica onto gibbsite, and Oelze et al. (2015) proposed a $\Delta_{eq}^{30}S_{SiO2,am\text{-}fluid}$ of around 0 ‰ based on amorphous silica precipitation experiments in the presence and absence of Al. The results of the present study, performed using the three-isotope method, which thereby verifies the attainment of isotopic equilibrium in the amorphous silica - aqueous solution system validates the results of these former studies. The three-isotope method was also adopted by Zheng et al. (2016) to assess the Si equilibrium fractionation factor between a Fe(III)-Si gel and an aqueous solution at pH 8. These authors report an equilibrium fractionation factor, $\Delta_{eq}^{30}Si_{SiO2,am\text{-}fluid}$ of -2.3 ± 0.23 ‰. The differences between this result and those reported in the present study are likely attributable to the substantial presence of Fe(III) in the solid phase ($X_{Fe(III)}/X_{Si} = 0.5$).

Many studies have shown that the absolute values of isotopic fractionation decreases as temperature increases (e.g. Urey, 1947; Bigeleisen, 1965; Schauble, 2004; Shahar et al., 2011; Huang et al., 2014). Such is also the case in the present study. At pH ~6 the $\Delta_{eq}^{30}Si_{SiO2,am\text{-}fluid}$ decreases from 0.45 ± 0.20 ‰ to 0.07 ± 0.06 ‰ as temperature increases from 25 to 75 °C. At more alkaline conditions, these fractionation factors also depend on pH due to the formation of additional Si aqueous species. As the stability of these aqueous species depends on temperature, the explicit account of their speciation as a function of temperature is required to accurately estimate equilibrium Si isotope fractionation factors.

5.2. Isotope fractionation among Si aqueous species

The combination of fluid speciation and measured equilibrium fractionation factors at 2 different pH allows the determination of the equilibrium fractionation among amorphous

504   silica, and the $H_4SiO_4^0$ and $H_3SiO_4^-$ aqueous species. The distinct equilibrium fractionation

505   factors among these species can be represented as $\Delta_{eq}{}^{30}Si_{SiO2,am\text{-}H_4SiO_4^0}$, $\Delta_{eq}{}^{30}Si_{SiO2,am\text{-}H_3SiO_4^-}$,

506   and $\Delta_{eq}{}^{30}Si_{H_3SiO_4^-\text{-}H_4SiO_4^0}$, and are listed in Table 4. Dupuis et al. (2015) estimated $\Delta_{eq}{}^{30}Si_{quartz\text{-}}$

507      $_{H_4SiO_4^0}$ from *ab initio* calculations, obtaining 2.1± 0.20 ‰ for 25°C. This value is somewhat

508   higher than that obtained between amorphous silica and this aqueous species in the present

509   study, $\Delta_{eq}{}^{30}Si_{SiO2,am\text{-}H_4SiO_4^0} = 0.45 \pm 0.20$ ‰. This difference can be explained by the different

510   structures of the solids. Quartz, with its continuous framework of SiO_4 tetrahedra, has an

511   ordered structure, which is not the case of the partially hydrated amorphous silica used in this

512   study. Therefore, the structural difference between quartz and aqueous $H_4SiO_4^0$ is more

513   important than that between amorphous silica and aqueous $H_4SiO_4^0$. As such, quartz is

514   expected to be enriched in ^{30}Si compared to amorphous silica.

515   The equilibrium Si isotope fractionation factor among the two major Si bearing

516   aqueous Si species, $\Delta_{eq}{}^{30}Si_{H_3SiO_4^-\text{-}H_4SiO_4^0}$, was found in the present study to be -2.34 ± 0.13 ‰

517   and -2.21 ± 0.05 ‰ at 25° and 75°C, respectively. These values can be directly compared to

518   the corresponding values determined using *ab initio* calculations. Dupuis et al. (2015)

519   reported that at 25°C, $\Delta_{eq}{}^{30}Si_{H_3SiO_4^-\text{-}H_4SiO_4^0} = -1.6 \pm 0.30$ ‰. In contrast, Fujii et al. (2015)

520   reported that at 25°C, $\Delta_{eq}{}^{30}Si_{H_3SiO_4^-\text{-}H_4SiO_4^0} = -3$ ‰. The value generated in the present study

521   falls between these calculated values.

522   The equilibrium Si isotope fractionation factor among the two major Si bearing

523   aqueous species determined in the present study can also be compared to that measured by

524   Fujii et al. (2015); this previous experimental study measured a 25°C $\Delta_{eq}{}^{30}Si_{H_3SiO_4^-\text{-}H_4SiO_4^0}$

525   equal to -3.5 ‰. The Fujii et al. (2015) study, however, took a different approach to determine

526   this equilibrium fractionation factor than that of the present study. Their method relied on the

527   purification of a Na_2SiO_4 solution at pH 9.4 by column chromatography using an anionic

528   resin. The two dominant Si aqueous species were collected in different elutions. These

529   elutions were then measured for their Si isotopic compositions. This approach allows running

530   experiments at much lower Si concentrations than those of the present study since there is no

531   need for the solutions to be in equilibrium with a solid Si-bearing phase. Note that at

532   amorphous silica-aqueous fluid equilibrium at pH >9, there is a possibility of the formation of

533   minor amounts of polynuclear Si bearing aqueous species (Dietzel, 2000) that could affect the

534   measured equilibrium isotopic fractionation between amorphous silica and its coexisting

535 aqueous fluid. The method used by Fuji et al. (2015) however, does not verify that isotopic

536 equilibrium is attained. Additionally, undefined fractionation may have occurred during the

537 column separation by sorption of Si on the anionic resin (Fuji et al., 2015).

538

539 **5.3. Kinetics of Si isotope exchange**

540   The first part of each experimental series began by dissolving amorphous SiO_2 to

541 equilibrium in its aqueous solution. The surface area normalized dissolution rates of these

542 experiments were retrieved by fitting these data to the rate equations (4) to (7). The rates,

543 reported in Table 3, range from 3.13×10^{-12} mol/m²/s at 25°C and pH 6 to 1.24×10^{-10}

544 mol/m²/s at 75°C and pH 9; these rates increase with increasing temperature and increasing

545 pH. They are similar to the dissolution rates of quartz obtained at corresponding temperature

546 and pH conditions by Brady and Walther (1989), Berger et al. (1994), and Icenhower and

547 Dove, (2000); these past reported values ranged from 10^{-12} to 10^{-13} mol/m²/s. Our values are

548 also similar to the amorphous silica and the phytoliths dissolution rates of 10^{-12} and 3×10^{-12}

549 mol/m²/s at 25°C, pH 5, and with comparable grain sizes reported by Plettnick et al. (1994)

550 and Fraysse et al. (2006), respectively. In contrast, our rates are substantially slower than that

551 of amorphous silica nanoparticles with a surface area of 232 m²/g at 25°C and pH 7 reported

552 by Diedrich et al. (2012).

553   The rates of isotopic equilibration provide some insight into the process controlling

554 isotopic equilibration. The variation of the degree of isotopic exchange (F) is plotted at a

555 function of time in Fig 7. The curves through the data points in this figure were generated

556 using the first order rate equation (Eqn. 16), to be consistent with the bulk dissolution rate

557 equation. The rate constants used for these calculations were obtained from the dissolution of

558 the amorphous silica during the first step of each experimental series. It can be seen in this

559 figure that the curves are close to, but somewhat lower than the F values during the first 10

560 days of reaction, when isotope exchange has progressed to 80-95%. The isotope exchange

561 rates tend to slow relative to that estimated using the corresponding bulk amorphous silica

562 dissolution rates as the systems approach isotopic equilibrium beyond this F value. This

563 behaviour suggests that the dominant rate-controlling mechanism of isotope equilibration in

564 the present study over the first 10 to 20 days of the isotopic equilibration is the detachment

565 and reattachment of silicic acid to and from the amorphous silica surface; note the system

566 during this isotopic equilibration is at bulk chemical equilibrium such that this coupled

567 attachment/detachment process does not result in net dissolution or precipitation. The

568 observations of the post-material solids by SEM and TEM suggest that the grains are
569 negligibly changed as a result of the isotope equilibration process. Such observations favour
570 the mechanism of an atomic-scale exchange of material at the solid-fluid interface rather than
571 the recrystallization of the solid.

572   The observation that the isotopic exchange rates match closely the bulk dissolution
573 rates measured during each isotopic exchange experimental series when F <80 to 95%
574 suggests that Si transport rate within the amorphous silica grains in this study is relatively fast
575 compared to the rate of detachment and attachment of SiO_2 at the surface for the bulk of the
576 isotopic exchange process over this time period. This fast isotope exchange rate is likely due
577 to the relatively small grain size of the amorphous SiO_2 used in the experiments; the average
578 grain size of these particles was 21 ± 5 nm. Based on the unit cell dimension of quartz, which
579 is ~ 5Å (Danielsson et al., 1976), it is likely that these grains are no more than ~40 unit cells
580 across. In addition, the presence of water in the amorphous silica structure may facilitate the
581 transport of Si into and out of these grains. Only after isotopic exchange has attained 80 to
582 90% of their equilibrium values do these exchange rates slow compared to bulk amorphous
583 silica dissolution rates. This may indicate that the final equilibration of the isotope exchange
584 reaction is becoming transport-limited near the end of each experimental series. Nevertheless,
585 all experimental series performed in this study approached isotopic equilibrium within the 55
586 to 360 days of each experimental series. If the rapid rate of the total Si isotopic equilibration
587 as observed here is also the case in natural ambient temperature systems, the preservation of
588 original Si isotopic signatures in natural fine-grained amorphous SiO_2 materials may be rare.
589

5.4. Can Si fractionation be used as a paleo pH and temperature proxy?
591   Fujii et al. (2015) proposed the use of Si isotope fractionation as a proxy of seawater
592 paleo-pH due to the pH-dependent concentration of the $H_3SiO_4^-$ and $H_4SiO_4^0$ species and the
593 consequent variation of solid-aqueous fluid fractionation factors with pH. Seawater however
594 has a pH of ~8 and thus mainly $H_4SiO_4^0$ will be present. As such, Si isotopes may be more
595 useful for determining pH in more alkaline environments. Numerous such environments can
596 be found in nature, for example in alkaline lakes (e.g. Mono Lake, California USA) or in
597 mafic/ultramafic rocks. The results of this study confirm the possibility of using Si isotopic
598 signatures in precipitated minerals as pH proxies of natural waters and provides the
599 equilibrium Si isotope fractionation factors between amorphous SiO_2, the dominant SiO_2
600 phase precipitating at ambient conditions with its coexisting aqueous solution at different pH.

601 The variation of amorphous SiO_2 – aqueous fluid fractionation factors determined as a
602 function of pH at 25° and 75°C using Eqn. (12) and the equilibrium fractionation factors from
603 this study are provided in Fig 8. Although the variation of this fractionation factor with pH is
604 substantially smaller than that of boron (Zeebe, 2005; Klochko et al., 2006; Noireaux et al.,
605 2015), as the Si does not change its coordination in aqueous inorganic systems, it has the
606 advantage of having a simpler and better-defined aqueous and solid speciation, potentially
607 making it a more precise tool for constraining some paleo-pH values. Note, however, that the
608 experiments presented in this study suggest that small (~20 nm) amorphous silica grains can
609 rapidly equilibrate with its co-existing aqueous fluid in the laboratory. Moreover amorphous
610 silica is hydrous; the presence of this water may facilitate Si transport within its structure. As
611 such further work should be made on the kinetics of isotopic exchange as a function solid
612 grain size and porosity, to assess the degree to which the Si isotope signatures of precipitated
613 amorphous SiO_2 are preserved over geologic timeframes.

614 The data obtained in this study not only show a variation in equilibrium Si isotope
615 fractionation depending on solution pH, but also on solution temperature. The equilibrium Si
616 isotope fractionation factor between amorphous SiO_2 and $H_4SiO_4^0$ at 75°C is significantly
617 lower than that at ambient temperature. Si isotopic fraction becomes more important at lower
618 temperatures. In Fig. 9, the equilibrium isotope fractionation factors of the present study at
619 neutral pH are extrapolated to 0 °C based on the polynomial function of Dupuis et al. (2015),
620 showing that a fractionation of ~0.9 ‰ can be expected at this temperature. This conclusion is
621 supported by the *ab initio* calculations of Dupuis et al. (2015) shown in Fig. 9, exhibiting a
622 much stronger fractionation factor between quartz and $H_4SiO_4^0$ as temperature decreases. This
623 relatively large fractionation factor at low temperature might explain the low $\delta^{30}Si$ signatures
624 found in Banded Iron Formations (BIFS, Chakrabarti et al., 2012) and/or the $\delta^{30}Si$ variation of
625 Archean cherts (Marin-Carbonne et al., 2012).

6. CONCLUSIONS

627 The results presented in this study confirm the significance of aqueous silica
628 speciation on equilibrium isotope fractionation between fluids and Si-bearing solids. The
629 equilibrium fractionation factor between amorphous SiO_2 and its co-existing aqueous solution
630 $\Delta_{eq}^{30}Si_{SiO2,am\text{-}fluid}$ at 25°C is 0.45 ± 0.20 ‰ at pH 6 and 1.63 ± 0.23 ‰ at pH 9.9. Using these
631 values and the distribution of the species in the aqueous solution, an equilibrium isotope
632 fractionation value between $H_3SiO_4^-$ and $H_4SiO_4^\circ$, $\Delta_{eq}^{30}Si_{H_3SiO_4^- - H_4SiO_4^0}$ = -2.34 ± 0.13 ‰ at

633 25°C was obtained. Such results suggest the possible use of the Si isotope signatures of
634 precipitated Si bearing minerals as a paleo pH proxy. Furthermore the Si isotopic
635 fractionation between amorphous silica and its coexisting aqueous fluid decreases with
636 increasing temperature, for example from 0.45 ± 0.20 ‰ at 25°C to 0.07 ± 0.06 ‰ at 75°C
637 and pH 6. It follows that the Si isotopic compositions of precipitated amorphous silica may
638 provide insight into the temperature of its formation.

639   This study also further validates the use of the three-isotope method as an effective
640 means to determine both the rates of isotope exchange and equilibrium isotope fractionation
641 factors. Such equilibrium fractionation factors facilitate greatly the interpretation of natural
642 isotope signatures. The rates of isotope exchange determined by this approach may also
643 provide new insight into both the mechanism of isotope exchange and the conditions at which
644 mineral isotopic signatures are best preserved in natural systems.

645

660

661

REFERENCES

662 Asael, D., Matthews, A., Oszczepalski, S., Bar-Matthews, M., Halicz, L., 2009. Fluid speciation controls of low temperature copper isotope fractionation applied to the Kupferschiefer and Timna ore deposits. Chem. Geol. 262, 147–158. https://doi.org/10.1016/j.chemgeo.2009.01.015

Balan, E., Noireaux, J., Mavromatis, V., Saldi, G.D., Montouillout, V., Blanchard, M., Pietrucci, F., Gervais, C., Rustad, J.R., Schott, J., Gaillardet, J., 2018. Theoretical isotopic fractionation between structural boron in carbonates and aqueous boric acid and borate ion. Geochim. Cosmochim. Acta 222, 117–129. https://doi.org/10.1016/j.gca.2017.10.017

Basile-Doelsch, I., Meunier, J.D., Parron, C., 2005. Another continental pool in the terrestrial silicon cycle. Nature 433, 399–402. https://doi.org/10.1038/nature03217

Beard, B.L., Handler, R.M., Scherer, M.M., Wu, L., Czaja, A.D., Heimann, A., Johnson, C.M., 2010. Iron isotope fractionation between aqueous ferrous iron and goethite. Earth Planet. Sci. Lett. 295, 241–250. https://doi.org/0.1016/j.epsl.2010.04.006

Berger, G., Cadore, E., Schott, J., Dove, P.M., 1994. Dissolution rate of quartz in lead and sodium electrolyte solutions between 25 and 300°C: Effect of the nature of surface complexes and reaction affinity. Geochim. Cosmochim. Acta 58, 541–551. https://doi.org/10.1016/0016-7037(94)90487-1

Bigeleisen, J., 1965. Chemistry of Isotopes: Isotope chemistry has opened new areas of chemical physics, geochemistry, and molecular biology. Science 147, 463–471. https://doi.org/10.1126/science.147.3657.463

Brady, P.V., Walther, J.V., 1989. Controls on silicate dissolution rates in neutral and basic pH solutions at 25°C. Geochim. Cosmochim. Acta 53, 2823–2830. https://doi.org/10.1016/0016-7037(89)90160-9

Brunauer, S., Emmett, P.H., Teller, E., 1938. Adsorption of Gases in Multimolecular Layers. J. Am. Chem. Soc. 60, 309–319. https://doi.org/10.1021/ja01269a023

Chakrabarti, R., Knoll, A.H., Jacobsen, S.B., Fischer, W.W., 2012. Si isotope variability in Proterozoic cherts. Geochim. Cosmochim. Acta 91, 187–201. https://doi.org/10.1016/j.gca.2012.05.025

Cole, D.R., Chakraborty, S., 2001. Rates and Mechanisms of Isotopic Exchange. Rev. Mineral. Geochem. 43, 83–223. https://doi.org/10.2138/gsrmg.43.1.83

Criss, R.., Gregory, R.., Taylor, H.., 1987. Kinetic theory of oxygen isotopic exchange between minerals and water. Geochim. Cosmochim. Acta 51, 1099–1108. https://doi.org/10.1016/0016-7037(87)90203-1

Danielsson, S., Grenthe, I., Oskarsson, å., 1976. A low-temperature apparatus for single-crystal diffractometry. The unit-cell dimension of α-quartz in the temperature range 86–298 K. J. Appl. Crystallogr. 9, 14–17. https://doi.org/10.1107/S0021889876010418

De La Rocha, C.L., Bescont, P., Croguennoc, A., Ponzevera, E., 2011. The silicon isotopic composition of surface waters in the Atlantic and Indian sectors of the Southern Ocean. Geochim. Cosmochim. Acta 75, 5283–5295. https://doi.org/10.1016/j.gca.2011.06.028

De La Rocha, C.L., Brzezinski, M.A., DeNiro, M.J., 2000. A first look at the distribution of the stable isotopes of silicon in natural waters. Geochim. Cosmochim. Acta 64, 2467–2477. https://doi.org/10.1016/S0016-7037(00)00373-2

708 De La Rocha, C.L., Brzezinski, M.A., DeNiro, M.J., Shemesh, A., 1998. Silicon-isotope
709   composition of diatoms as an indicator of past oceanic change. Nature 395, 680–683.
710   https://doi.org/10.1038/27174

711 Delstanche, S., Opfergelt, S., Cardinal, D., Elsass, F., André, L., Delvaux, B., 2009. Silicon
712   isotopic fractionation during adsorption of aqueous monosilicic acid onto iron oxide.
713   Geochim. Cosmochim. Acta 73, 923–934. https://doi.org/10.1016/j.gca.2008.11.014

714 Delvigne, C., Cardinal, D., Hofmann, A., André, L., 2012. Stratigraphic changes of Ge/Si,
715   REE+Y and silicon isotopes as insights into the deposition of a Mesoarchaean banded
716   iron formation. Earth Planet. Sci. Lett. 355–356, 109–118.
717   https://doi.org/10.1016/j.epsl.2012.07.035

718 Demarest, M.S., Brzezinski, M.A., Beucher, C.P., 2009. Fractionation of silicon isotopes
719   during biogenic silica dissolution. Geochim. Cosmochim. Acta 73, 5572–5583.
720   https://doi.org/10.1016/j.gca.2009.06.019

721 Diedrich, T., Dybowska, A., Schott, J., Valsami-Jones, E., Oelkers, E.H., 2012. The
722   Dissolution Rates of SiO_2 Nanoparticles As a Function of Particle Size. Environ. Sci.
723   Technol. 46, 4909–4915. https://doi.org/10.1021/es2045053

724 Dietzel, M., 2000. Dissolution of silicates and the stability of polysilicic acid. Geochim.
725   Cosmochim. Acta 64, 3275–3281. https://doi.org/10.1016/S0016-7037(00)00426-9

726 Ding, T.P., Gao, J.F., Tian, S.H., Wang, H.B., Li, M., 2011. Silicon isotopic composition of
727   dissolved silicon and suspended particulate matter in the Yellow River, China, with
728   implications for the global silicon cycle. Geochim. Cosmochim. Acta 75, 6672–6689.
729   https://doi.org/10.1016/j.gca.2011.07.040

730 Ding, T.P., Ma, G.R., Shui, M.X., Wan, D.F., Li, R.H., 2005. Silicon isotope study on rice
731   plants from the Zhejiang province, China. Chem. Geol. 218, 41–50.
732   https://doi.org/10.1016/j.chemgeo.2005.01.018

733 Ding, T.P., Tian, S.H., Sun, L., Wu, L.H., Zhou, J.X., Chen, Z.Y., 2008a. Silicon isotope
734   fractionation between rice plants and nutrient solution and its significance to the study
735   of the silicon cycle. Geochim. Cosmochim. Acta 72, 5600–5615.
736   https://doi.org/10.1016/j.gca.2008.09.006

737 Ding, T.P., Zhou, J.X., Wan, D.F., Chen, Z.Y., Wang, C.Y., Zhang, F., 2008b. Silicon isotope
738   fractionation in bamboo and its significance to the biogeochemical cycle of silicon.
739   Geochim. Cosmochim. Acta 72, 1381–1395. https://doi.org/10.1016/j.gca.2008.01.008

740 Douthitt, C.., 1982. The geochemistry of the stable isotopes of silicon. Geochim. Cosmochim.
741   Acta 46, 1449–1458. https://doi.org/10.1016/0016-7037(82)90278-2

742 Dupuis, R., Benoit, M., Nardin, E., Méheut, M., 2015. Fractionation of silicon isotopes in
743   liquids: The importance of configurational disorder. Chem. Geol. 396, 239–254.
744   https://doi.org/10.1016/j.chemgeo.2014.12.027

745 Frierdich, A.J., Beard, B.L., Scherer, M.M., Johnson, C.M., 2014. Determination of the
746   Fe(II)aq–magnetite equilibrium iron isotope fractionation factor using the three-
747   isotope method and a multi-direction approach to equilibrium. Earth Planet. Sci. Lett.
748   391, 77–86. https://doi.org/10.1016/j.epsl.2014.01.032

749 Frings, P.J., Clymans, W., Fontorbe, G., Gray, W., Chakrapani, G.J., Conley, D.J., De La
750   Rocha, C., 2015. Silicate weathering in the Ganges alluvial plain. Earth Planet. Sci.
751   Lett. 427, 136–148. https://doi.org/10.1016/j.epsl.2015.06.049

752 Fujii, T., Moynier, F., Blichert-Toft, J., Albarède, F., 2014. Density functional theory
753   estimation of isotope fractionation of Fe, Ni, Cu, and Zn among species relevant to
754   geochemical and biological environments. Geochim. Cosmochim. Acta 140, 553–576.
755   https://doi.org/10.1016/j.gca.2014.05.051

756 Fujii, T., Pringle, E.A., Chaussidon, M., Moynier, F., 2015. Isotope fractionation of Si in
757   protonation/deprotonation reaction of silicic acid: A new pH proxy. Geochim.
758   Cosmochim. Acta 168, 193–205. https://doi.org/10.1016/j.gca.2015.07.003

759 Geilert, S., Vroon, P.Z., Roerdink, D.L., Van Cappellen, P., van Bergen, M.J., 2014. Silicon
760   isotope fractionation during abiotic silica precipitation at low temperatures: Inferences
761   from flow-through experiments. Geochim. Cosmochim. Acta 142, 95–114.
762   https://doi.org/10.1016/j.gca.2014.07.003

763 Georg, R.B., Reynolds, B.C., Frank, M., Halliday, A.N., 2006. New sample preparation
764   techniques for the determination of Si isotopic compositions using MC-ICPMS.
765   Chem. Geol. 235, 95–104. https://doi.org/10.1016/j.chemgeo.2006.06.006

766 Georg, R.B., Reynolds, B.C., West, A.J., Burton, K.W., Halliday, A.N., 2007. Silicon isotope
767   variations accompanying basalt weathering in Iceland. Earth Planet. Sci. Lett. 261,
768   476–490. https://doi.org/10.1016/j.epsl.2007.07.004

769 Georg, R.B., Zhu, C., Reynolds, B.C., Halliday, A.N., 2009. Stable silicon isotopes of
770   groundwater, feldspars, and clay coatings in the Navajo Sandstone aquifer, Black
771   Mesa, Arizona, USA. Geochim. Cosmochim. Acta 73, 2229–2241.
772   https://doi.org/10.1016/j.gca.2009.02.005

773 Grasse, P., Ehlert, C., Frank, M., 2013. The influence of water mass mixing on the dissolved
774   Si isotope composition in the Eastern Equatorial Pacific. Earth Planet. Sci. Lett. 380,
775   60–71. https://doi.org/10.1016/j.epsl.2013.07.033

776 He, H., Zhang, S., Zhu, C., Liu, Y., 2016. Equilibrium and kinetic Si isotope fractionation
777   factors and their implications for Si isotope distributions in the Earth's surface
778   environments. Acta Geochim. 35, 15–24. https://doi.org/10.1007/s11631-015-0079-x

779 Hemming, N.G., Hanson, G.N., 1992. Boron isotopic composition and concentration in
780   modern marine carbonates. Geochim. Cosmochim. Acta 56, 537–543.
781   https://doi.org/10.1016/0016-7037(92)90151-8

782 Hendry, K.R., Leng, M.J., Robinson, L.F., Sloane, H.J., Blusztjan, J., Rickaby, R.E.M.,
783   Georg, R.B., Halliday, A.N., 2011. Silicon isotopes in Antarctic sponges: an
784   interlaboratory comparison. Antarct. Sci. 23, 34–42.
785   https://doi.org/10.1017/S0954102010000593

786 Hendry, K.R., Robinson, L.F., 2012. The relationship between silicon isotope fractionation in
787   sponges and silicic acid concentration: Modern and core-top studies of biogenic opal.
788   Geochim. Cosmochim. Acta 81, 1–12. https://doi.org/10.1016/j.gca.2011.12.010

789 Holloway, J.M., Nordstrom, D.K., Böhlke, J.K., McCleskey, R.B., Ball, J.W., 2011.
790   Ammonium in thermal waters of Yellowstone National Park: Processes affecting
791   speciation and isotope fractionation. Geochim. Cosmochim. Acta 75, 4611–4636.
792   https://doi.org/10.1016/j.gca.2011.05.036

793 Huang, F., Wu, Z., Huang, S., Wu, F., 2014. First-principles calculations of equilibrium
794   silicon isotope fractionation among mantle minerals. Geochim. Cosmochim. Acta 140,
795   509–520. https://doi.org/10.1016/j.gca.2014.05.035

796 Huang, T.-C., Tsai, F.-N., 1970. Kinetic studies on the isotopic exchange of calcium ion and
797   calcium carbonate. J. Inorg. Nucl. Chem. 32, 17–31. https://doi.org/10.1016/0022-
798   1902(70)80445-6

799 Icenhower, J.P., Dove, P.M., 2000. The dissolution kinetics of amorphous silica into sodium
800   chloride solutions: effects of temperature and ionic strength. Geochim. Cosmochim.
801   Acta 64, 4193–4203. https://doi.org/10.1016/S0016-7037(00)00487-7

802 Jiskra, M., Wiederhold, J.G., Bourdon, B., Kretzschmar, R., 2012. Solution Speciation
803   Controls Mercury Isotope Fractionation of Hg(II) Sorption to Goethite. Environ. Sci.
804   Technol. 46, 6654–6662. https://doi.org/10.1021/es3008112

805 Johnson, C.M., Skulan, J.L., Beard, B.L., Sun, H., Nealson, K.H., Braterman, P.S., 2002.
806   Isotopic fractionation between Fe(III) and Fe(II) in aqueous solutions. Earth Planet.
807   Sci. Lett. 195, 141–153. https://doi.org/10.1016/S0012-821X(01)00581-7
808 Kathrin Abraham, Opfergelt, S., Fripiat, F., Cavagna, A.-J., de Jong, J.T.M., Foley, S.F.,
809   André, L., Cardinal, D., 2008. $\delta^{30}Si$ and $\delta^{29}Si$ Determinations on USGS BHVO-1 and
810   BHVO-2 Reference Materials with a New Configuration on a Nu Plasma Multi-
811   Collector ICP-MS. Geostand. Geoanalytical Res. 32, 193–202.
812   https://doi.org/10.1111/j.1751-908X.2008.00879.x
813 Klochko, K., Cody, G.D., Tossell, J.A., Dera, P., Kaufman, A.J., 2009. Re-evaluating boron
814   speciation in biogenic calcite and aragonite using 11B MAS NMR. Geochim.
815   Cosmochim. Acta 73, 1890–1900. https://doi.org/10.1016/j.gca.2009.01.002
816 Klochko, K., Kaufman, A.J., Yao, W., Byrne, R.H., Tossell, J.A., 2006. Experimental
817   measurement of boron isotope fractionation in seawater. Earth Planet. Sci. Lett. 248,
818   276–285. https://doi.org/10.1016/j.epsl.2006.05.034
819 Li, W., Beard, B.L., Johnson, C.M., 2011. Exchange and fractionation of Mg isotopes
820   between epsomite and saturated MgSO4 solution. Geochim. Cosmochim. Acta 75,
821   1814–1828. https://doi.org/10.1016/j.gca.2011.01.023
822 Li, Y., Ding, T., Wan, D., 1995. Experimental study of silicon isotope dynamic fractionation
823   and its application in geology. Chin. J. Geochem. 14, 212–219.
824   https://doi.org/10.1007/BF02842044
825 Marin-Carbonne, J., Chaussidon, M., Robert, F., 2012. Micrometer-scale chemical and
826   isotopic criteria (O and Si) on the origin and history of Precambrian cherts:
827   Implications for paleo-temperature reconstructions. Geochim. Cosmochim. Acta 92,
828   129–147. https://doi.org/10.1016/j.gca.2012.05.040
829 Marin-Carbonne, J., Robert, F., Chaussidon, M., 2014. The silicon and oxygen isotope
830   compositions of Precambrian cherts: A record of oceanic paleo-temperatures?
831   Precambrian Res. 247, 223–234. https://doi.org/10.1016/j.precamres.2014.03.016
832 Matsuhisa, Y., Goldsmith, J.R., Clayton, R.N., 1978. Mechanisms of hydrothermal
833   crystallization of quartz at 250°C and 15 kbar. Geochim. Cosmochim. Acta 42, 173–
834   182. https://doi.org/10.1016/0016-7037(78)90130-8
835 Matthews, A., Goldsmith, J.R., Clayton, R.N., 1983a. On the mechanisms and kinetics of
836   oxygen isotope exchange in quartz and feldspars at elevated temperatures and
837   pressures. Geol. Soc. Am. Bull. 94, 396. https://doi.org/10.1130/0016-
838   7606(1983)94<396:OTMAKO>2.0.CO;2
839 Matthews, A., Goldsmith, J.R., Clayton, R.N., 1983b. Oxygen isotope fractionations
840   involving pyroxenes: The calibration of mineral-pair geothermometers. Geochim.
841   Cosmochim. Acta 47, 631–644. https://doi.org/10.1016/0016-7037(83)90284-3
842 Matthews, A., Goldsmith, J.R., Clayton, R.N., 1983c. Oxygen isotope fractionation between
843   zoisite and water. Geochim. Cosmochim. Acta 47, 645–654.
844 Mavromatis, V., González, A.G., Dietzel, M., Schott, J., 2019. Zinc isotope fractionation
845   during the inorganic precipitation of calcite - Towards a new pH proxy. Geochim.
846   Cosmochim. Acta 244, 99-112.
847 Noireaux, J., Mavromatis, V., Gaillardet, J., Schott, J., Montouillout, V., Louvat, P., Rollion-
848   Bard, C., Neuville, D.R., 2015. Crystallographic control on the boron isotope paleo-
849   pH proxy. Earth Planet. Sci. Lett. 430, 398–407.
850   https://doi.org/10.1016/j.epsl.2015.07.063
851 Oelze, M., von Blanckenburg, F., Bouchez, J., Hoellen, D., Dietzel, M., 2015. The effect of
852   Al on Si isotope fractionation investigated by silica precipitation experiments. Chem.
853   Geol. 397, 94–105. https://doi.org/10.1016/j.chemgeo.2015.01.002

854   Oelze, M., von Blanckenburg, F., Hoellen, D., Dietzel, M., Bouchez, J., 2014. Si stable
855   isotope fractionation during adsorption and the competition between kinetic and
856   equilibrium isotope fractionation: Implications for weathering systems. Chem. Geol.
857   380, 161–171. https://doi.org/10.1016/j.chemgeo.2014.04.027

858   Opfergelt, S., Cardinal, D., André, L., Delvigne, C., Bremond, L., Delvaux, B., 2010.
859   Variations of δ30Si and Ge/Si with weathering and biogenic input in tropical basaltic
860   ash soils under monoculture. Geochim. Cosmochim. Acta 74, 225–240.
861   https://doi.org/10.1016/j.gca.2009.09.025

862   Opfergelt, S., Cardinal, D., Henriet, C., André, L., Delvaux, B., 2006. Silicon isotope
863   fractionation between plant parts in banana: In situ vs. in vitro. J. Geochem. Explor.
864   88, 224–227. https://doi.org/10.1016/j.gexplo.2005.08.044

865   Opfergelt, S., Georg, R.B., Delvaux, B., Cabidoche, Y.-M., Burton, K.W., Halliday, A.N.,
866   2012. Silicon isotopes and the tracing of desilication in volcanic soil weathering
867   sequences, Guadeloupe. Chem. Geol. 326–327, 113–122.
868   https://doi.org/10.1016/j.chemgeo.2012.07.032

869   Opfergelt, S., Williams, H.M., Cornelis, J.T., Guicharnaud, R.A., Georg, R.B., Siebert, C.,
870   Gislason, S.R., Halliday, A.N., Burton, K.W., 2017. Iron and silicon isotope behaviour
871   accompanying weathering in Icelandic soils, and the implications for iron export from
872   peatlands. Geochim. Cosmochim. Acta 217, 273–291.
873   https://doi.org/10.1016/j.gca.2017.08.033

874   Platzner, I.T. (Itzhak T., Habfast, K., Walder, A.J., Goetz, A., 1997. Modern isotope ratio
875   mass spectrometry, Chemical analysis. J. Wiley, Chichester ; New York.

876   Plettnick, S., Chou, L., Wollast, R., 1994. Kinetics and mechanisms of dissolution of silica at
877   room temperature and pressure. Mineral. Mag. 58A.

878   Pogge von Strandmann, P.A.E., Opfergelt, S., Lai, Y.-J., Sigfússon, B., Gislason, S.R.,
879   Burton, K.W., 2012. Lithium, magnesium and silicon isotope behaviour
880   accompanying weathering in a basaltic soil and pore water profile in Iceland. Earth
881   Planet. Sci. Lett. 339–340, 11–23. https://doi.org/10.1016/j.epsl.2012.05.035

882   Poitrasson, F., 2017. Silicon Isotope Geochemistry. Rev. Mineral. Geochem. 82, 289–344.
883   https://doi.org/10.2138/rmg.2017.82.8

884   Pokrovski, G.S., Schott, J., 1998. Experimental study of the complexation of silicon and
885   germanium with aqueous organic species: implications for germanium and silicon
886   transport and Ge/Si ratio in natural waters. Geochim. Cosmochim. Acta 62, 3413–
887   3428. https://doi.org/10.1016/S0016-7037(98)00249-X

888   Pokrovsky, O.S., Reynolds, B.C., Prokushkin, A.S., Schott, J., Viers, J., 2013. Silicon isotope
889   variations in Central Siberian rivers during basalt weathering in permafrost-dominated
890   larch forests. Chem. Geol. 355, 103–116.
891   https://doi.org/10.1016/j.chemgeo.2013.07.016

892   Reddy, T.R., Frierdich, A.J., Beard, B.L., Johnson, C.M., 2015. The effect of pH on stable
893   iron isotope exchange and fractionation between aqueous Fe(II) and goethite. Chem.
894   Geol. 397, 118–127. https://doi.org/10.1016/j.chemgeo.2015.01.018

895   Reynolds, B., Frank, M., Halliday, A., 2006. Silicon isotope fractionation during nutrient
896   utilization in the North Pacific. Earth Planet. Sci. Lett. 244, 431–443.
897   https://doi.org/10.1016/j.epsl.2006.02.002

898   Rimstidt, J.D., Barnes, H.L., 1980. The kinetics of silica-water reactions. Geochim.
899   Cosmochim. Acta 44, 1683–1699. https://doi.org/10.1016/0016-7037(80)90220-3

900   Riotte, J., Meunier, J.-D., Zambardi, T., Audry, S., Barboni, D., Anupama, K., Prasad, S.,
901   Chmeleff, J., Poitrasson, F., Sekhar, M., Braun, J.-J., 2018a. Processes controlling
902   silicon isotopic fractionation in a forested tropical watershed: Mule Hole Critical Zone

Observatory (Southern India). Geochim. Cosmochim. Acta 228, 301–319. https://doi.org/10.1016/j.gca.2018.02.046

Riotte, J., Sandhya, K., Prakash, N.B., Audry, S., Zambardi, T., Chmeleff, J., Buvaneshwari, S., Meunier, J.-D., 2018b. Origin of silica in rice plants and contribution of diatom Earth fertilization: insights from isotopic Si mass balance in a paddy field. Plant Soil 423, 481–501. https://doi.org/10.1007/s11104-017-3535-z

Roerdink, D.L., van den Boorn, S.H.J.M., Geilert, S., Vroon, P.Z., van Bergen, M.J., 2015. Experimental constraints on kinetic and equilibrium silicon isotope fractionation during the formation of non-biogenic chert deposits. Chem. Geol. 402, 40–51. https://doi.org/10.1016/j.chemgeo.2015.02.038

Russell, W.A., Papanastassiou, D.A., Tombrello, T.A., 1978. Ca isotope fractionation on the Earth and other solar system materials. Geochim. Cosmochim. Acta 42, 1075–1090. https://doi.org/10.1016/0016-7037(78)90105-9

Ryan, B.M., Kirby, J.K., Degryse, F., Harris, H., McLaughlin, M.J., Scheiderich, K., 2013. Copper speciation and isotopic fractionation in plants: uptake and translocation mechanisms. New Phytol. 199, 367–378. https://doi.org/10.1111/nph.12276

Savage, P.S., Armytage, R.M.G., Georg, R.B., Halliday, A.N., 2014. High temperature silicon isotope geochemistry. Lithos 190–191, 500–519. https://doi.org/10.1016/j.lithos.2014.01.003

Savage, P.S., Georg, R.B., Williams, H.M., Halliday, A.N., 2013. The silicon isotope composition of the upper continental crust. Geochim. Cosmochim. Acta 109, 384–399. https://doi.org/10.1016/j.gca.2013.02.004

Schindelin, J., Arganda-Carreras, I., Frise, E., Kaynig, V., Longair, M., Pietzsch, T., Preibisch, S., Rueden, C., Saalfeld, S., Schmid, B., Tinevez, J.-Y., White, D.J., Hartenstein, V., Eliceiri, K., Tomancak, P., Cardona, A., 2012. Fiji: an open-source platform for biological-image analysis. Nat. Methods 9, 676–682. https://doi.org/10.1038/nmeth.2019

Schott, J., Mavromatis, V., Fujii, T., Pearce, C.R., Oelkers, E.H., 2016. The control of carbonate mineral Mg isotope composition by aqueous speciation: Theoretical and experimental modeling. Chem. Geol. 445, 120–134. https://doi.org/10.1016/j.chemgeo.2016.03.011

Schuessler, J.A., von Blanckenburg, F., 2014. Testing the limits of micro-scale analyses of Si stable isotopes by femtosecond laser ablation multicollector inductively coupled plasma mass spectrometry with application to rock weathering. Spectrochim. Acta Part B At. Spectrosc. 98, 1–18. https://doi.org/10.1016/j.sab.2014.05.002

Shahar, A., Hillgren, V.J., Young, E.D., Fei, Y., Macris, C.A., Deng, L., 2011. High-temperature Si isotope fractionation between iron metal and silicate. Geochim. Cosmochim. Acta 75, 7688–7697. https://doi.org/10.1016/j.gca.2011.09.038

Shahar, A., Young, E.D., Manning, C.E., 2008. Equilibrium high-temperature Fe isotope fractionation between fayalite and magnetite: An experimental calibration. Earth Planet. Sci. Lett. 268, 330–338. https://doi.org/10.1016/j.epsl.2008.01.026

Steinhoefel, G., von Blanckenburg, F., Horn, I., Konhauser, K.O., Beukes, N.J., Gutzmer, J., 2010. Deciphering formation processes of banded iron formations from the Transvaal and the Hamersley successions by combined Si and Fe isotope analysis using UV femtosecond laser ablation. Geochim. Cosmochim. Acta 74, 2677–2696. https://doi.org/10.1016/j.gca.2010.01.028

Truesdale, V.W., LeCorre, P., 1975. Manuel d'analyse des sels nuritifs dans l'eau de mer: Utilisation de L'autoanalyzer II technicon (r). Université de Bretagne occiendtale, France.

Urey, H.C., 1947. The thermodynamic properties of isotopic substances. J. Chem. Soc. Resumed 562. https://doi.org/10.1039/jr9470000562

van den Boorn, S.H.J.M., van Bergen, M.J., Vroon, P.Z., de Vries, S.T., Nijman, W., 2010. Silicon isotope and trace element constraints on the origin of ~3.5Ga cherts: Implications for Early Archaean marine environments. Geochim. Cosmochim. Acta 74, 1077–1103. https://doi.org/10.1016/j.gca.2009.09.009

Welch, S.A., Beard, B.L., Johnson, C.M., Braterman, P.S., 2003. Kinetic and equilibrium Fe isotope fractionation between aqueous Fe(II) and Fe(III). Geochim. Cosmochim. Acta 67, 4231–4250. https://doi.org/10.1016/S0016-7037(03)00266-7

Wischmeyer, A.G., De La Rocha, C.L., Maier-Reimer, E., Wolf-Gladrow, D.A., 2003. Control mechanisms for the oceanic distribution of silicon isotopes. Glob. Biogeochem. Cycles 17, n/a-n/a. https://doi.org/10.1029/2002GB002022

Wu, L., Percak-Dennett, E.M., Beard, B.L., Roden, E.E., Johnson, C.M., 2012. Stable iron isotope fractionation between aqueous Fe(II) and model Archean ocean Fe–Si coprecipitates and implications for iron isotope variations in the ancient rock record. Geochim. Cosmochim. Acta 84, 14–28. https://doi.org/10.1016/j.gca.2012.01.007

Yin, R., Feng, X., Wang, J., Li, P., Liu, J., Zhang, Y., Chen, J., Zheng, L., Hu, T., 2013. Mercury speciation and mercury isotope fractionation during ore roasting process and their implication to source identification of downstream sediment in the Wanshan mercury mining area, SW China. Chem. Geol. 336, 72–79. https://doi.org/10.1016/j.chemgeo.2012.04.030

Young, E.D., Galy, A., Nagahara, H., 2002. Kinetic and equilibrium mass-dependent isotope fractionation laws in nature and their geochemical and cosmochemical significance. Geochim. Cosmochim. Acta 66, 1095–1104. https://doi.org/10.1016/S0016-7037(01)00832-8

Zambardi, T., Poitrasson, F., 2011. Precise Determination of Silicon Isotopes in Silicate Rock Reference Materials by MC-ICP-MS. Geostand. Geoanalytical Res. 35, 89–99. https://doi.org/10.1111/j.1751-908X.2010.00067.x

Zeebe, R.E., 2005. Stable boron isotope fractionation between dissolved $B(OH)_3$ and $B(OH)_4^-$. Geochim. Cosmochim. Acta 69, 2753–2766. https://doi.org/10.1016/j.gca.2004.12.011

Zhang, J., Quay, P.D., Wilbur, D.O., 1995. Carbon isotope fractionation during gas-water exchange and dissolution of CO_2. Geochim. Cosmochim. Acta 59, 107–114. https://doi.org/10.1016/0016-7037(95)91550-D

Zheng, X.-Y., Beard, B.L., Reddy, T.R., Roden, E.E., Johnson, C.M., 2016. Abiologic silicon isotope fractionation between aqueous Si and Fe(III)–Si gel in simulated Archean seawater: Implications for Si isotope records in Precambrian sedimentary rocks. Geochim. Cosmochim. Acta 187, 102–122. https://doi.org/10.1016/j.gca.2016.05.012

Ziegler, K., Chadwick, O.A., Brzezinski, M.A., Kelly, E.F., 2005a. Natural variations of δ30Si ratios during progressive basalt weathering, Hawaiian Islands. Geochim. Cosmochim. Acta 69, 4597–4610. https://doi.org/10.1016/j.gca.2005.05.008

Ziegler, K., Chadwick, O.A., White, A.F., Brzezinski, M.A., 2005b. δ30Si systematics in a granitic saprolite, Puerto Rico. Geology 33, 817. https://doi.org/10.1130/G21707.1

996

998   Fig. 1. Distribution of aqueous Si species in equilibrium with amorphous silica as a function

999   of pH calculated with PHREEQC using its llnl database, for A. 25°C and B. 75°C. Notice that

1000   at 75°C the increase in the concentration of the $H_3SiO_4^-$ species occurs at a lower pH than at

1001   25°C.

1002

1003   Fig. 2. Schematic diagram of the three-isotope method applied to Si, modified after Li et al.

1004   (2011) and Zheng et al. (2016). At time (t) zero, and in the absence of isotopic exchange

1005   (shown in %), Phase A plots as the isotopically "normal" component on the terrestrial

1006   fractionation line (TFL). At t_0 Phase B shows a distinct offset from the TFL as it is enriched

1007   in ^{29}Si. The isotopic composition of phases A and B gradually evolve towards 100% isotopic

1008   exchange. The lines connecting the two phases at a given time always cross the system

1009   average as required by isotope mass balance. When isotopic exchange is complete, the two

1010   phases plot on a secondary fractionation line, whose position is dictated by the isotopic mass

1011   balance of the system.

1012

1013   Fig. 3. Representative images of amorphous SiO_2 powders. A) SEM image of the initial

1014   powder showing agglomerates of amorphous SiO_2 grains. B) TEM image of the initial powder

1015   showing rounded ~ 21 nm SiO_2 grains. C) Representative SEM image of reacted amorphous

1016   silica powder. D) TEM image of reacted amorphous silica recovered from the longest

1017   duration experiment performed at T ~25°C, pH ~6.

1018

1019   Fig. 4. Temporal evolution of dissolved Si concentration during the equilibration of the initial

1020   reactive fluids with amorphous silica during the first step of each experimental series. The

1021   dashed lines represent a fit of the data using Eqn. 7 with values of rate constant k'- listed in

1022   Table 3.

1023

1024   Fig. 5.Plots of pH, Si concentrations and isotopic compositions of solid and fluid phases as a

1025   function of time during the second step of each experimental series. The 2 S.D. uncertainties

1026   of data points are denoted by the error bars. Initial values are represented by dashed lines with

1027   their 2 S.D. error envelope shaded in grey. A) pH= 6.4 at 25 °C, B) pH= 9.9 at 25 °C, C) 5.8

1028   at 75 °C, and D) 9.1 at 75 °C.

1029

1030

1031 Fig. 6. Plots of the isotopic composition of the solid and fluid phases as a function of the
1032 degree of isotope exchange during the second step of each experimental series. A) pH= 6.4 at
1033 25 °C , B) pH= 9.9 at 25 °C, C) 5.8 at 75 °C, and D) 9.1 at 75 °C. Excluded data from the fit
1034 are shown by grey symbols – see text.

1035

1036 Fig. 7. The temporal evolution of the degree of isotopic exchange F during the four
1037 experimental series runs of this study. Dashed lines are generated assuming a first order rate
1038 law (Eqn. 16), using the dissolution rate constants from the amorphous silica dissolution rate
1039 experiments performed as the first step of each experimental series.

1040

1041 Fig. 8. Si equilibrium fractionation factors between amorphous silica and the fluid at 25°C
1042 and 75°C as a function of pH calculated using the Si equilibrium fractionation factors derived
1043 in the present study together with the aqueous speciation of Si shown in Fig 1. The curves in
1044 this figure are dashed at elevated pH as this calculation does not take into account polyatomic
1045 Si aqueous complexes, which may become important at these conditions.

1046

1047 Fig. 9. Si equilibrium fractionation factors between quartz (Dupuis et al., 2015) and
1048 amorphous silica and $H_4SiO_4^o$ (this study) as a function of temperature. Red dotted describes
1049 extrapolated values.

1050

1051

1052 **TABLE CAPTIONS**

1053 Table 1. Summary of the initial conditions of the first step of each experimental series
1054 performed in the present study. Quantity in grams of fluids and solids used are denoted as
1055 $m_{initial\ sol}$ and $m_{SiO_2,am}$.

1056

1057 Table 2. Overview of the results of the isotopic exchange experiments performed in this
1058 study. Uncertainties of the isotopic measurements are expressed as 2 SD (Standard
1059 Deviation), and 2 SE (Standard Error). The 2 SE is computed following the relation:
1060 $SE = \frac{SD}{\sqrt{(n-1)}} \times t$, where n denotes the number of measurements performed, and t denotes the

1061 Student t-factor (Platzner et al., 1997). δ_{eq} represents the equilibrium isotopic composition of
1062 ^{29}Si and F denotes the degree of isotopic exchange. [a] denotes the spiked initial solution.

1063

1064 Table 3. Concentration of aqueous Si in equilibrium with amorphous silica and dissolution
1065 rate constants and rates obtained from the first step of the four experimental series runs in this
1066 study.

1067

1068 Table 4. Average aqueous Si-speciation during the second step of each experimental series
1069 run in this study together with the resulting isotopic fractionation factors between solid and
1070 solution, solid and the $H_4SiO_4^0$ and $H_3SiO_4^-$ species, and between $H_3SiO_4^-$ and $H_4SiO_4^0$
1071 species.

1072

1073 Table 5. Initial isotopic exchange rates, calculated from the first 10 days of isotope exchange
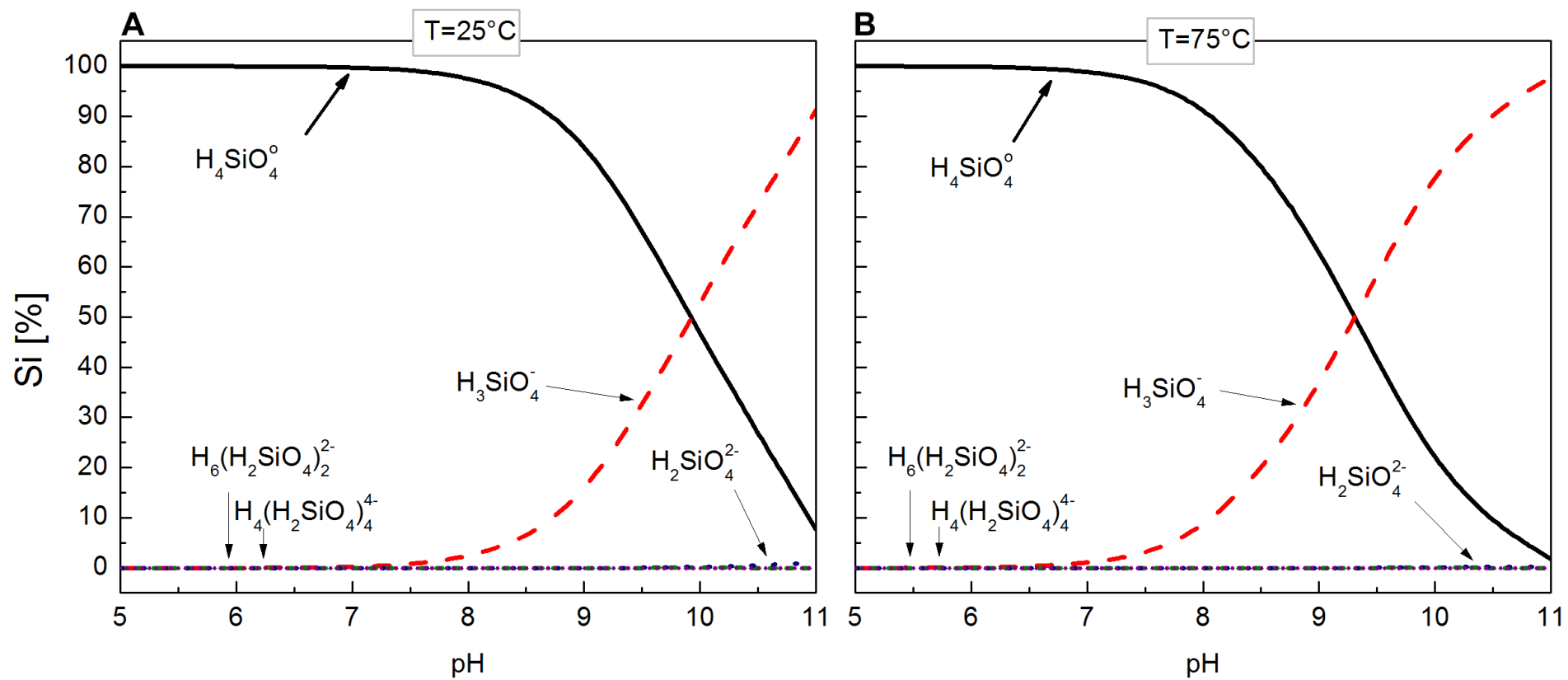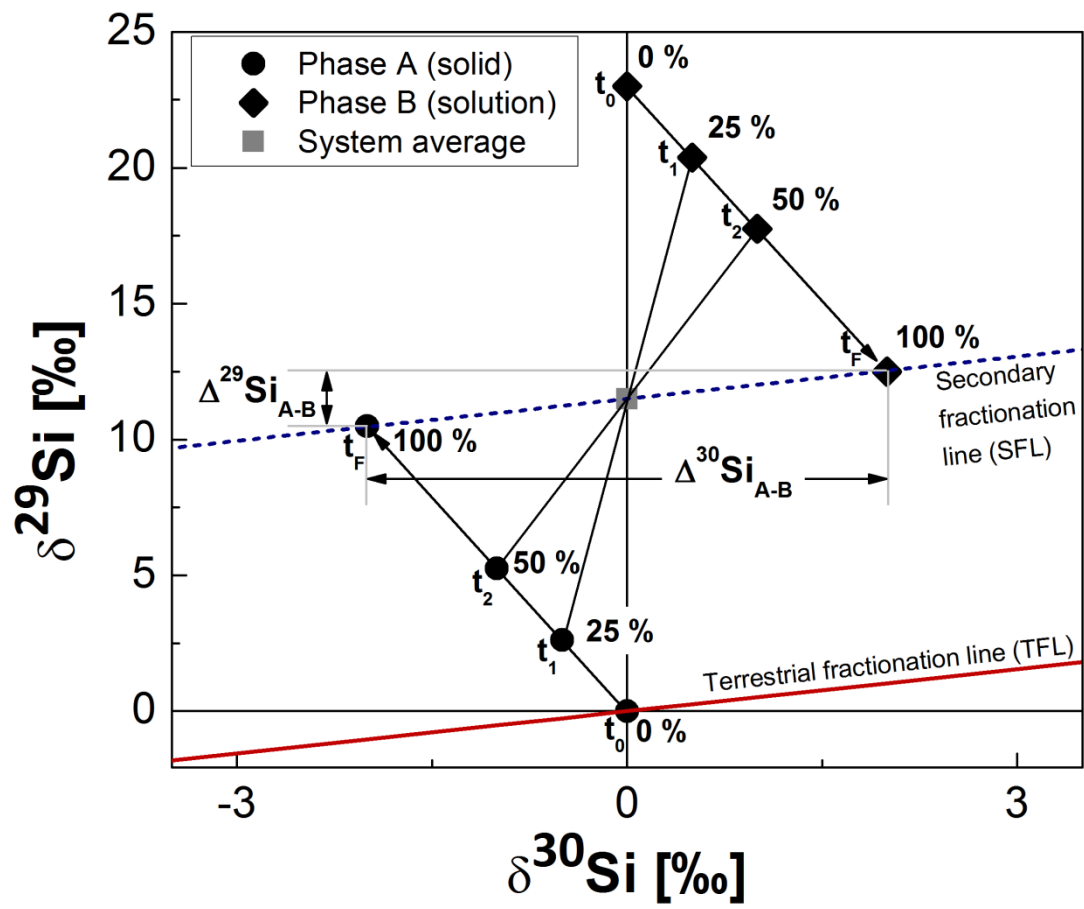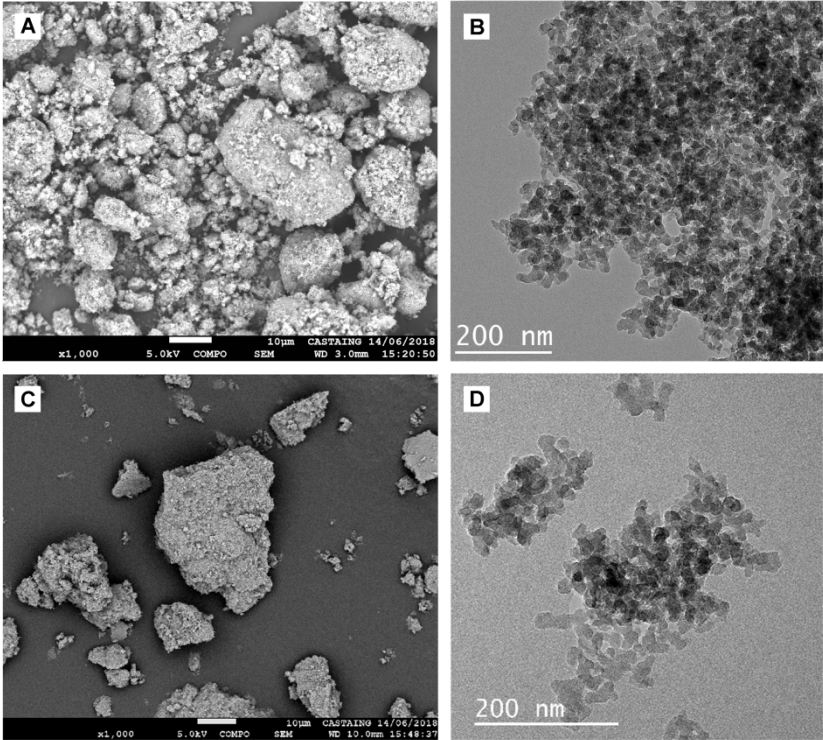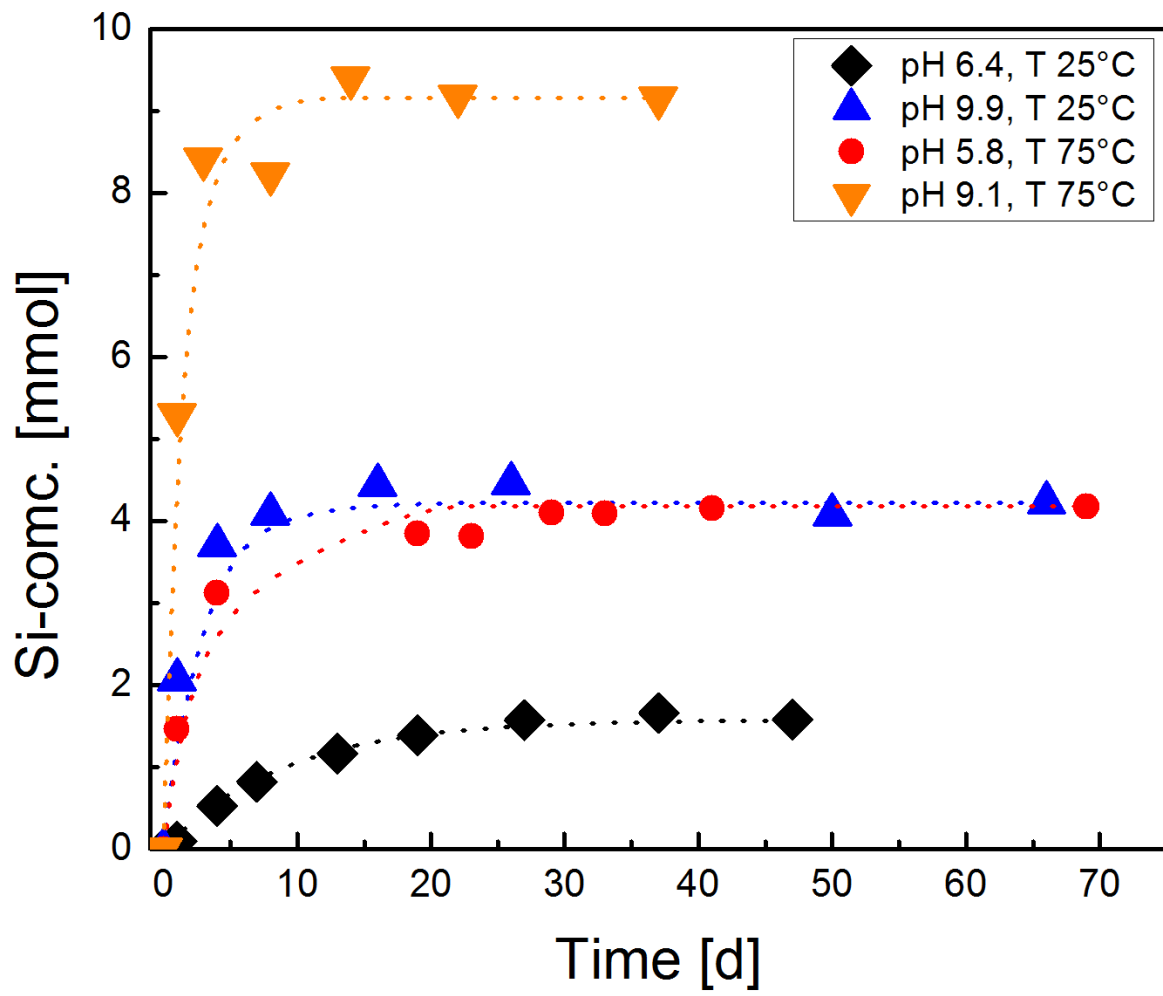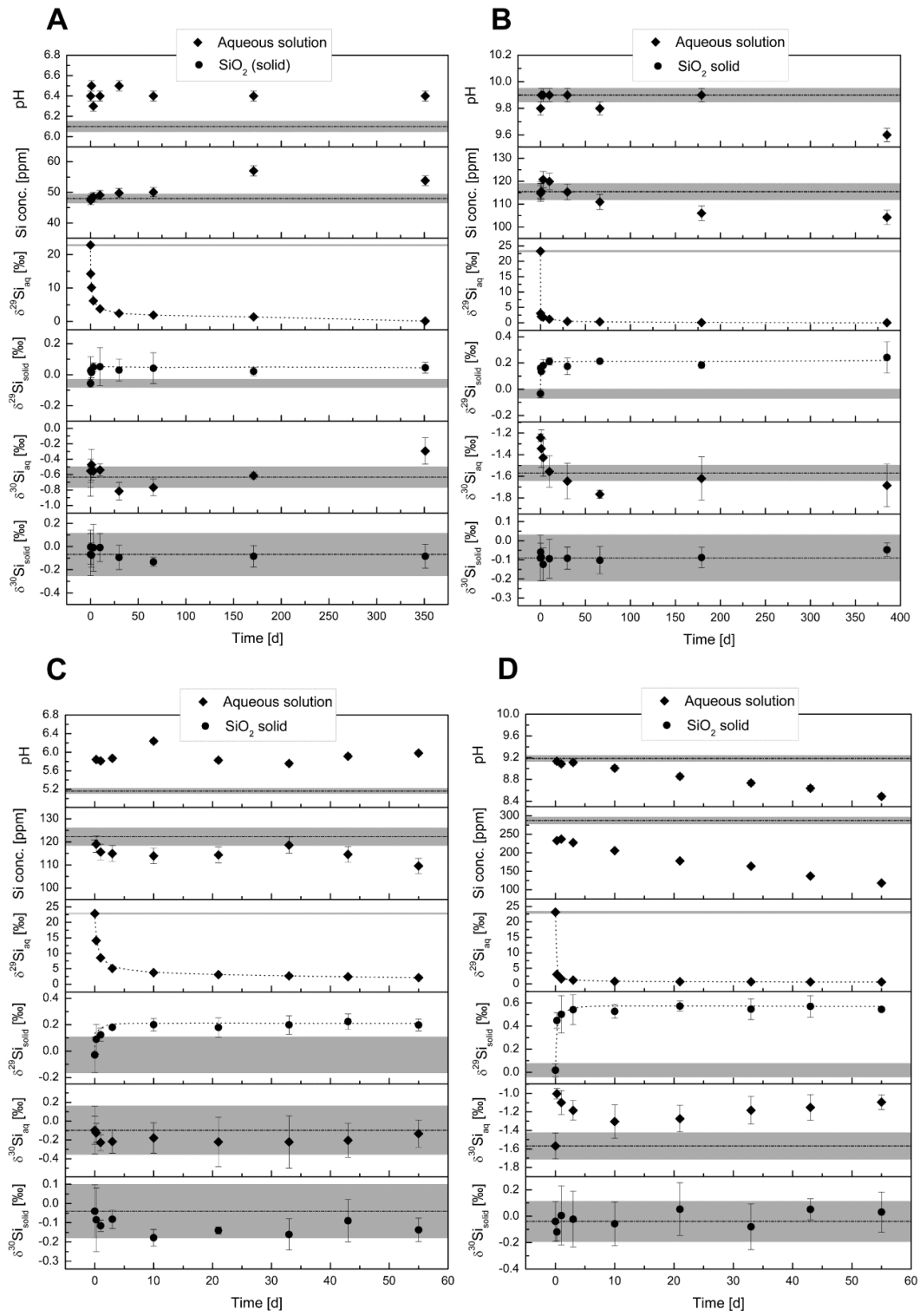1074 based on a first order rate law.
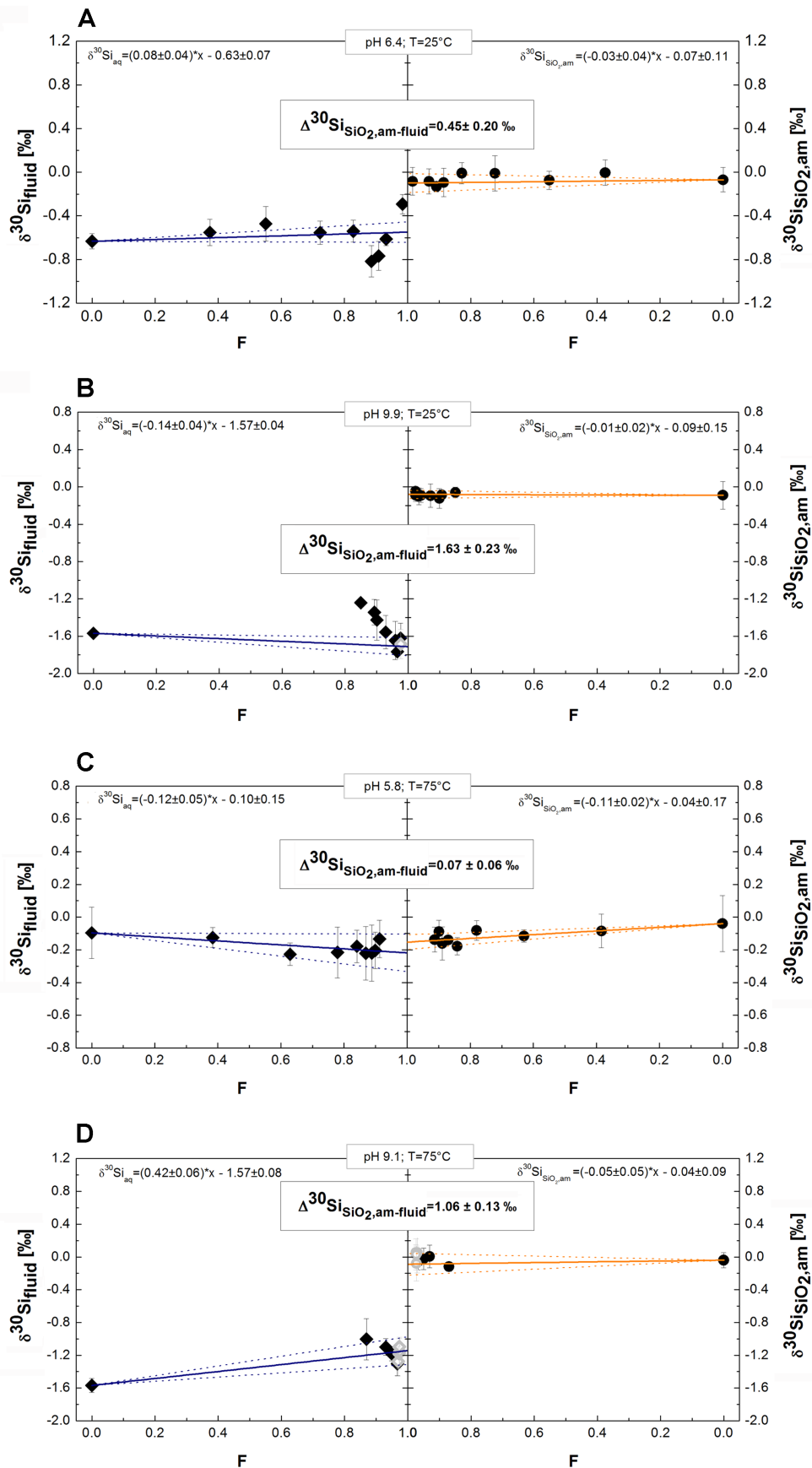
Fig. 1.

Fig. 2.

Fig. 3.

Fig. 4.

Fig. 5.

Fig. 6.

Fig.7.
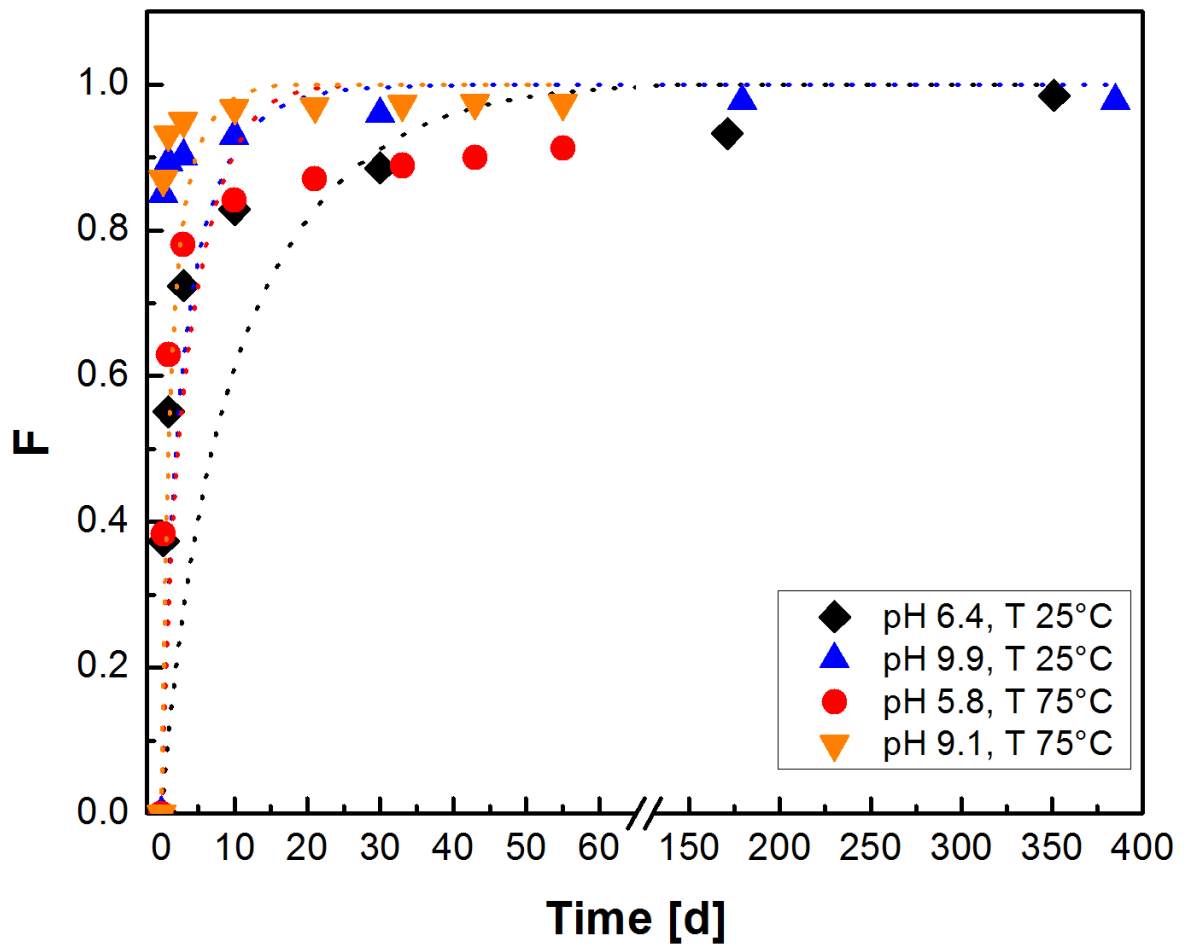
Fig. 8.
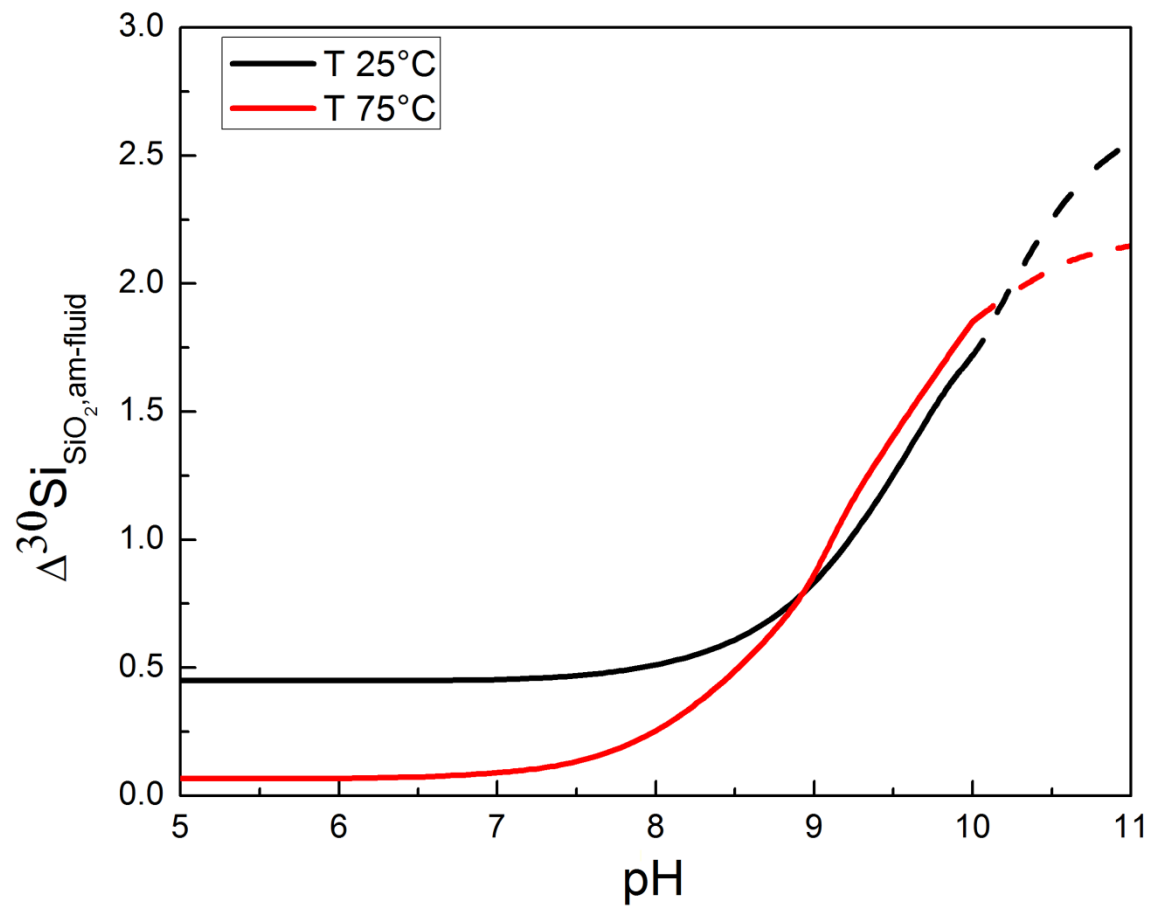
Fig. 9.

Table A
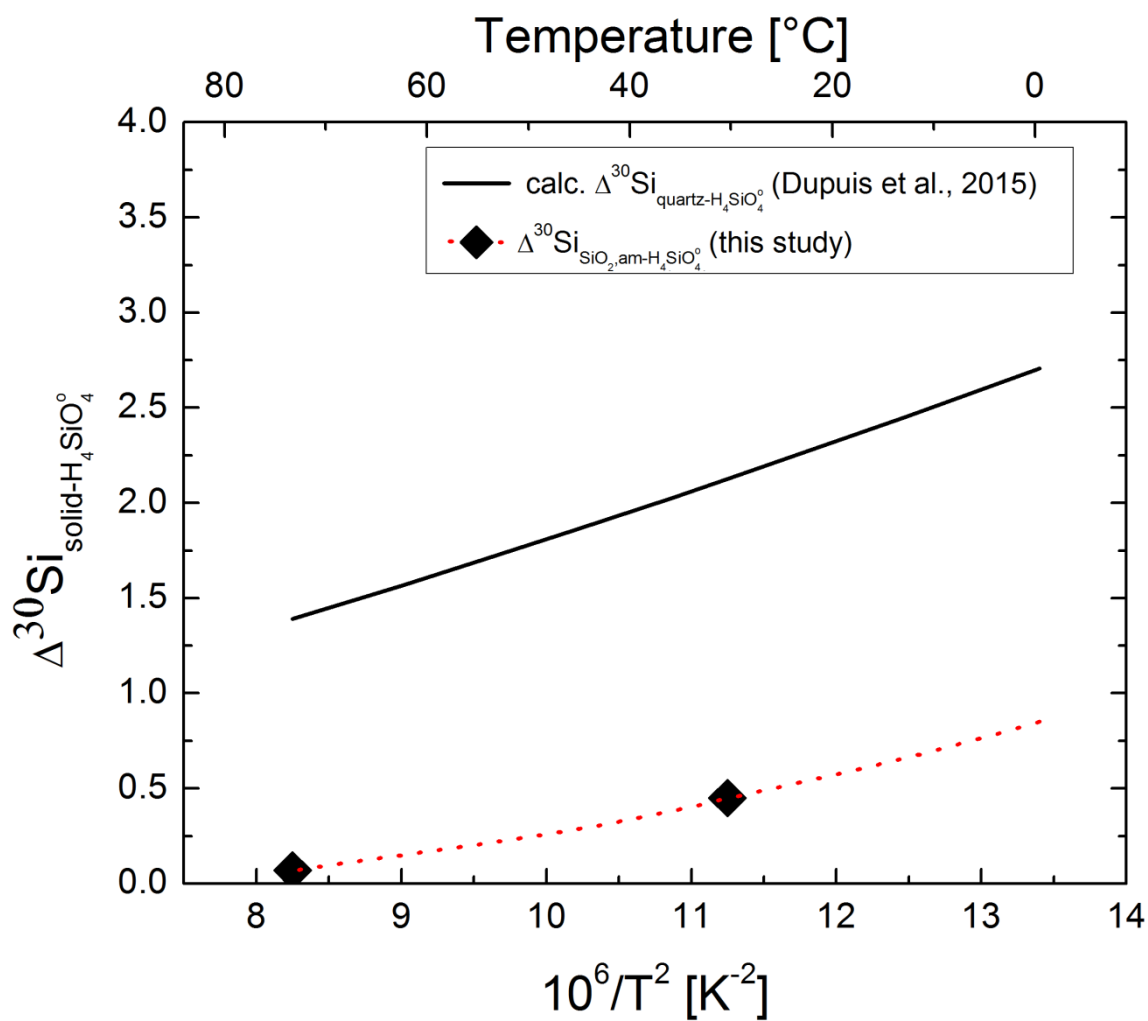
Exp.	Temperature [°C]	Time [d]	pH	Si-conc. [ppm]	Si-conc. [mmol/kg]
SibA:					
	25	0	8.7	0.00	0.00
	25	1	5.5	2.71	0.10
	25	4	6.6	14.75	0.53
	25	7	6.0	23.07	0.82
	25	13	6.8	32.80	1.17
	25	19	6.6	39.02	1.39
	25	27	6.7	44.18	1.57
	25	37	6.4	46.69	1.66
	25	47	6.2	44.40	1.58
SicB:					
	25	0	10.2	0.00	0.00
	25	1	10.2	58.18	2.07
	25	4	10.2	104.08	3.71
	25	8	10.2	114.93	4.09
	25	16	10.2	124.72	4.44
	25	26	10.1	125.19	4,46
	25	50	10.2	114.73	4.08
	25	66	10.1	118.66	4.22
Sig75A:					
	75	0	5.9	0.00	0.00
	75	1	6.4	41.12	1.46
	75	4	6.5	87.67	3.12
	75	19	5.8	108.03	3.85
	75	23	5.7	107.12	3.81
	75	29	5.8	115.10	4.10
	75	33	5.7	114.91	4.09
	75	41	5.7	116.65	4.15
	75	69	5.7	117.35	4.18
Sik75B:					
	75	0	9.25	0.00	0.00
	75	1	10.02	148.71	5.29
	75	3	9.4	236.23	8.41
	75	8	9.9	231.37	8.24
	75	14	9.3	264.18	9.41
	75	22	9.3	257.85	9.18
	75	37	9.3	257.35	9.16

Table B

sample	Temp. [°C]	run time [d]	S_{BET} [m^2/g]	grain size [nm]	m_{H2O} [wt %]	chemical formula
SibA 8	25	351	137.1	20.86	9.4	$SiO_2 \cdot 0.33\ H_2O$
SicB 8	25	385	164.1	20.69	8.6	$SiO_2 \cdot 0.34\ H_2O$
Sig75A 8	75	55	171.7	19.60	8.1	$SiO_2 \cdot 0.28\ H_2O$
Sik75B 6	75	33	119.0	n.a.	7.5	$SiO_2 \cdot 0.32\ H_2O$

TABLE CAPTION ELECTRONIC SUPPLEMENT

Table A: Temporal evolution of dissolved Si concentration and pH during equilibration of the initial Si-free reactive fluids with the pre-treated amorphous silica.

Table B: Summary of the measured characteristics of the reacted solids collected after the longest duration experiment for the experiments at 25°C and pH 5.8 at 75°C. Longest reacted powder available at time of analysis at pH 9.1 and 75°C after 33 days.